Journal of ENERGY TECHNOLOGY

Journal of
ENERGY TECHNOLOGY

VOLUME 10 / Issue 4

JOURNAL OF ENERGY TECHNOLOGY

Spoštovani bralci revije Journal of energy technology (JET)

Jedrska energetika omogoča učinkovito proizvodnjo električne in toplotne energije. V svetu je trenutno delujočih približno 450 jedrskih reaktorjev za proizvodnjo električne energije, razen tega deluje v svetu še približno 225 raziskovalnih reaktorjev, cca. 180 jedrskih reaktorjev je uporabljenih za pogon ladij in podmornic. Na ta način se v svetu pridobi približno 11 % električne energije ter dobršen del toplotne energije in energije potrebne za pogon ladij ter podmornic. Absolutno največ električne energije s pomočjo jedrskih reaktorjev pridobijo v ZDA, Rusiji in Franciji. V Franciji je delež proizvedene električne energije z jedrsko energetiko približno 75 %. Slovenija spada v skupino šestnajstih držav z vsaj 25 % deležem elektrike proizvedene v jedrskih elektrarnah. Razvoj jedrskih tehnologij na področju fuzije in fisije je zelo intenziven. Z novejšimi generacijami jedrskih reaktorjev bo možno še učinkoviteje in varneje pridobivati toplotno, električno energijo ter vodik. V predstavljenem izvodu revije je objavljen tudi članek, ki obravnava omenjeno tematiko.

<div align="right">

Jurij AVSEC
odgovorni urednik revije JET

</div>

Dear Readers of the Journal of Energy Technology (JET)

Nuclear energy enables the efficient production of electricity and heat. There are currently approximately 450 nuclear reactors operating in the world, with an additional approximately 225 research reactors in the world. Furthermore, about 180 nuclear reactors powered ships and submarines. In this way, around 11% of the electricity is supplied to the world as well as a good part of the heat and energy needed for the propulsion of ships and submarines. Overwhelmingly, most of the electricity generated by nuclear reactors is in the USA, Russia, and France. In France, the share of electricity produced by nuclear energy technology is approximately 75%. Slovenia belongs to a group of sixteen countries in which at least 25% of the electricity is produced in nuclear power plants. The development of technologies in fusion and fission is very intense. With newer generations of nuclear reactors, it will be possible to generate heat, electricity and hydrogen more efficiently and safely. An article published in this issue is dealing with this topic.

Jurij AVSEC
Editor-in-chief of JET

Table of Contents /
Kazalo

Journal of Energy Technology

A STRAIGHTFORWARD ANALYTICAL WAY OF EVALUATING THE SINGLE-PHASE INVERTER SPWM FREQUENCY SPECTRUM

ANALITIČEN POSTOPEK OCENITVE FREKVENČNEGA SPEKTRA SPWM IZHODNE NAPETOSTI ENOFAZNEGA RAZMERNIKA

Alenka Hren[1ℜ], Franc Mihalič[2]

Keywords: Fourier analysis, sinusoidal pulse-width modulation (SPWM), over-modulation phenomenon, single-phase inverter, total harmonic distortion (THD)

Abstract

For a DC-AC converter (inverter), a key element in renewable power supply systems, an output voltage of sinusoidal shape is required to assure a high-quality sustainable energy flow. Thus, through the modulation process, this property must be "incorporated" into the output voltage. This operation incurs some harmonic distortion into the inverter output voltage, which can have an undesired influence on the load. In the single- or three-phase systems (grid-connected, uninterrupted power supply systems (UPS) or motor drives), the high quality Total Harmonic Distortion (THD) factor must be considered; the voltage harmonic content also must be limited.

This paper provides a comprehensive spectrum analysis of a three-level output voltage in single-phase inverter. The output voltage is generated by triangular Sinusoidal Pulse-Width Modulation (SPWM) and, by using the Fourier analysis, Bessel functions and trigonometric equality, the high

---

[1ℜ] Corresponding author: dr. Alenka Hren, Tel.: +386 2 220 7332, Mailing address: University of Maribor, Faculty of Electrical Engineering and Computer Science, Koroška cesta 46, 2000 Maribor, E-mail address: alenka.hren@um.si

[2] dr. Franc Mihalič, University of Maribor, Faculty of Electrical Engineering and Computer Science, Koroška cesta 46, 2000 Maribor, E-mail address: franc.mihalic@um.si

harmonic components are extracted in a straightforward analytical way. Finally, the over-modulation phenomenon is also considered, and the procedure is experimentally validated.

Povzetek

Za zagotavljanje visokokakovostnega trajnostnega pretoka energije iz obnovljivih virov, mora razmerniško vezje, ki je ključni sestavni element pretvorniških sistemov, na izhodu zagotavljat sinusno obliko napetosti. To lastnost oz. obliko "vgradimo" v izhodno napetost razsmernika z izbranim modulacijskih postopkom, ki pa ob osnovni harmonski kompenenti vnaša v izhodno napetost tudi višje harmonske komponente. Te negativno vplivajo na breme razsmerniškega vezja in njegov izkoristek delovanja. V enofaznem ali trifaznem sistem (omrežne povezave, sistemi neprekinjenega napajanja ali motorni pogoni), mora razmerniško vezje delovati tudi z ustreznim, dovolj majhnim, faktorjem popačitve (Total Harmonic Distortion – THD), ki pa je odvisen prav od vsebnosti višjih harmonskih komponent v izhodni napetosti.

V članku je opisan postopek celovite analize harmonskega spektra trinivojske izhodne napetosti enofaznega razsmernika, pri čemer izhodno trinivojsko napetost generiramo s pomočjo sinusne trikotne modulacije (Sinusoidal Pulse-Width Modulation - SPWM). Z uporabo Fourierjeve analize, Besselovih funkcij in trigonometričnih enakosti lahko posamezne višje harmonske komponente izračunamo analitično. Opisan je tudi način delovanja razsmernika in postopek izračuna harmonskih komponent v področju nadmodulacije. Pravilnost postopka analitičnega izračuna je eksperimentalno verificirana.

1   INTRODUCTION

The efficiency and stable operation of switching mode power inverters are of crucial importance for the sustainable production of the renewable energy sources connected to the utility grid, [1], [2], or that are a part of the standalone multifunctional power systems, [3], and are both closely related to the used modulation strategy. The Pulse-Width Modulation (PWM) strategy has been in a focus of research for many decades, [4], and remains an active research topic, [5], [6], due to its widespread usage in many fields of applications. Its usage is the most popular in the control of switching mode power converters for which it continues to represent a state-of-the-art solution.

Although, PWM has been used for many years and is well-described in many textbooks, [7]–[10], the PWM algorithms for switching power converters have been the subject of intensive research, [11]–[15], and some initiations of the analytical approach have been established, especially in [11]. Some PWM research work has been dedicated to the analytical way to understand the ac-ac converter modulation strategies, [12], [16], [17]. The necessity of the analysis of the PWM strategies in single-phase inverters began with the exploitation of the back-up systems (UPS) and with taking advantage of acoustics equipment in home appliances, [18]–[23]. Single-phase inverters in back-up systems are designed to adapt to the changing needs of load and input voltage sources, and the filter function can be solved by using passive filters, [7]. To minimize the filters' weight and size, it is also important to know the harmonic components of the inverter output voltage. Finally, it is generally accepted that the performance of an inverter that operates with arbitrary switching strategy is closely related to the frequency spectrum of its output voltage, [11].

PWM can be implemented in many different forms. Pulse frequency is the most important parameter related to the PWM method and can be either constant or variable. A constant frequency PWM signal is obtained by comparing the modulation function with the carrier signal that can be in a sawtooth or a triangular shape. The most commonly used PWM form for a single-phase inverter is a naturally sampled PWM with a triangular (double-edge) carrier signal and a sinusoid as a modulation function, known as SPWM, since this kind of PWM improves the harmonic content of the pulse train considerably, *[24]*.

In many textbooks, the authors only describe the "modern" approach for frequency spectrum evaluation based on Fast Fourier Transformation (FFT), probably due to the comfortability of this sophisticated mathematical tool. Understanding the PWM process using FFT was explored as a short-cut due to its spread appearance in many computer software tools, such as Matlab, LabVIEW SPICE, EWB, Simplorer, among others. These algorithms are also available in some electronic measuring instruments.

This paper presents a step-by-step analytical approach to the exact evaluation of single-phase inverter frequency spectrum obtained by naturally sampled SPWM. The proposed analytical way of evaluating SPWM frequency spectrum gives a comprehensive and deep insight into the mechanism of the harmonic components generation as well as a better foundation for understanding or even designing the SPWM devices in inverters. The main goal is to follow the SPWM procedure exactly by using the Fourier analysis, Bessel functions, and trigonometric equality in order to extract the high harmonic components in an analytical way. The switching (existing) function introduced by Wood, *[9]*, is used for a mathematical description of the modulation function. Additionally, the over-modulation phenomenon in a single-phase inverter and its analysis are considered and are presented in Section 3, where the obtained results were also experimentally verified in order to prove the procedure's correctness. Conclusions are summarized in Section 4.

2   SINGLE-PHASE FULL-BRIDGE INVERTER

When the high-efficiency, low-cost, and compact structure are of primary concern, the transformer-less inverter's topologies based on bridge configuration are the primary choice. Fig. 1 shows a single-phase full-bridge inverter circuit with a DC input voltage (v_{in}) and AC output voltage (v_{out}), the semiconductor switches' structure and the load structure. The inverter consists of two legs (half-bridges) with two semiconductor switches (IGBTs or MOSFETs and diode as indicated in Fig. 1), voltage sources indicated by ($V_d/2$) and current source (indicated by Load), representing the inverter output filter consisting of inductor L, capacitor C, and load resistance R.

The SPWM processes can generally be divided into two groups with respect to the inverter output voltage that can be either in two-level (+V_d and −V_d) or three-level shape (with +V_d, 0 and −V_d). Since it is well known that the three-level output voltage has better spectrum properties, this kind of SPWM process will be considered in detail in this paper. Moreover, the first harmonic magnitude can be increased over V_d when over-modulation is applied, which means that the modulation index must exceed 1. With over-modulation, an increased magnitude of the first harmonic component is welcome in those situations in which the input voltage is decreased, but as a consequence of this phenomenon, *[10]*, additional spectrum lines appear, which also increases the Total Harmonic Distortion (THD) of the output signal.
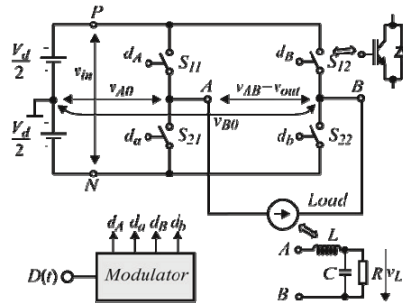
Figure 1: *Single-phase inverter structure; the semiconductor switch structure; the (current source) load structure.*
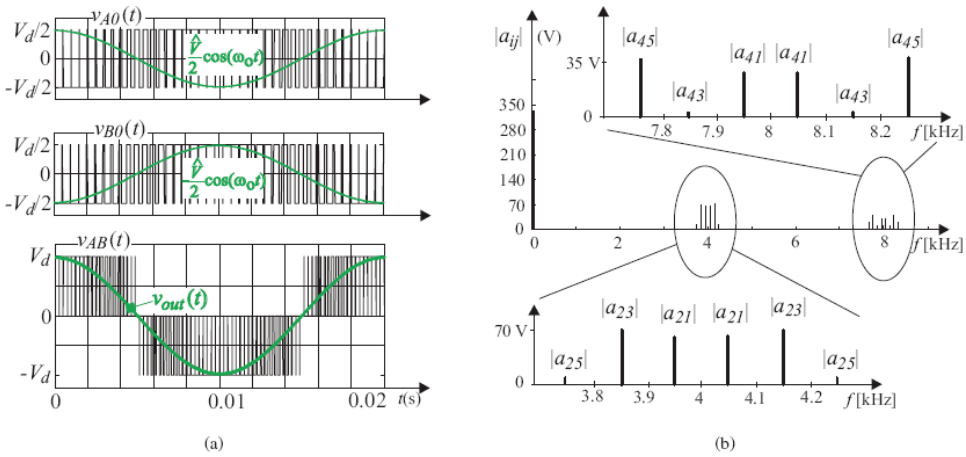
Figure 2: *(a) Output voltages: $v_{A0}(t)$, $v_{B0}(t)$ and $v_{AB}(t)$ with appropriate modulation functions and (b) Spectral lines for three-level output voltage.*

2.1 Generation of Three-Level Output Voltage

The whole inverter shown in Fig. 1 is divided into two half-bridge structures (legs). By using the first leg (switches S_{11} and S_{21}) the voltage $v_{A0}(t)$ ("first leg" voltage) and by using the second one (switches S_{12} and S_{22}) the voltage $v_{B0}(t)$ ("second leg" voltage) are generated at the inverter output, both with respect to the neutral point (shown in Fig. 1 and Fig. 2(a), respectively). If voltage $v_{A0}(t)$ precedes $v_{B0}(t)$ for an appropriate phase angle the inverter output voltage $v_{AB}(t)$ that equals the difference between voltages $v_{A0}(t)$ and $v_{B0}(t)$ will have the desired magnitude and desired three-level waveform, as indicated in Fig. 2(a). Voltages $v_{A0}(t)$ and $v_{B0}(t)$ are described as two switching events:

$$v_{A0}(t) = d_A(t)(V_d/2) + d_a(t)(-V_d/2), \qquad (2.1)$$

$$v_{B0}(t) = d_B(t)(V_d/2) + d_b(t)(-V_d/2), \qquad (2.2)$$

where the switching functions (see Fig. 3(a) and 3(b)) are:
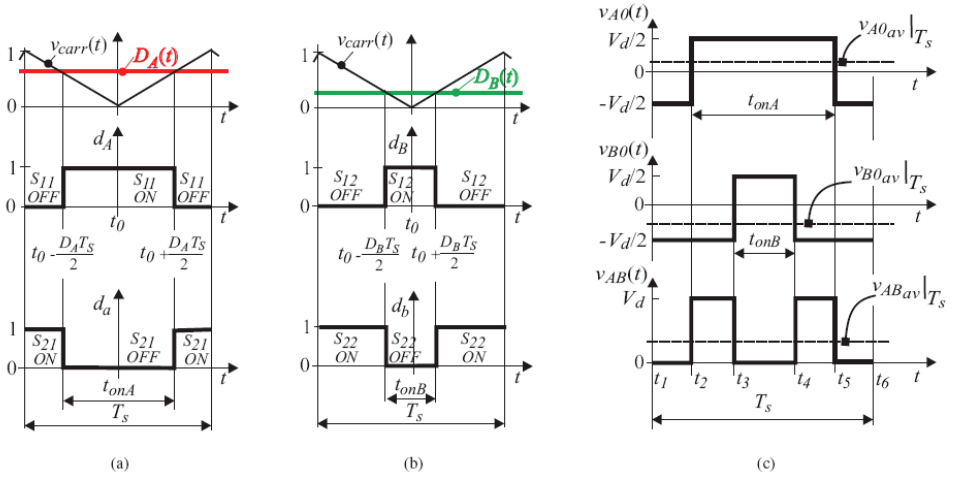
Figure 3: *Three-level switching functions generation (a,b) and, output voltages on the interval T_S (c): $v_{A0}(t)$, $v_{B0}(t)$ and $v_{AB}(t)$.*

$$d_A = \begin{cases} 1, & S_{11} = ON, \\ 0, & S_{11} = OFF, \end{cases} \quad d_a = \begin{cases} 1, & S_{21} = ON, \\ 0, & S_{21} = OFF, \end{cases} \tag{2.3}$$

$$d_B = \begin{cases} 1, & S_{12} = ON, \\ 0, & S_{12} = OFF, \end{cases} \quad d_b = \begin{cases} 1, & S_{22} = ON, \\ 0, & S_{22} = OFF. \end{cases} \tag{2.4}$$

In order to avoid the short circuit between the battery terminals P and N, the following conditions must be fulfilled:

$$d_A(t) + d_a(t) = 1, \tag{2.5}$$

$$d_B(t) + d_b(t) = 1. \tag{2.6}$$

Applying the above conditions in (2.1) and (2.2) follows to:

$$v_{A0}(t) = (2d_A(t) - 1)(V_d/2), \tag{2.7}$$

$$v_{B0}(t) = (2d_B(t) - 1)(V_d/2). \tag{2.8}$$

Referring to Fig. 3(c) (up and in the middle), the average value of the voltages vA0(t) and vB0(t) over the interval [0,Ts] can be evaluated as:

$$v_{A0}\Big|_{av}\Big|_{T_s} = \frac{1}{T_s} \int_{t1}^{t6} v_{A0}(t)dt = (2D_A(t) - 1)V_d / 2, \tag{2.9}$$

$$v_{B0}\Big|_{av}\Big|_{T_s} = \frac{1}{T_s} \int_{t1}^{t6} v_{B0}(t)dt = (2D_B(t) - 1)V_d / 2, \tag{2.10}$$

where $D_A(t) = t_{onA}/T_s$ and $D_B(t) = t_{onB}/T_s$ represent the corresponding duty cycle functions. If $T_s \ll T = 2\pi/\omega_o$ holds, the following approximation can be introduced:

$$\left. v_{A0_{av}}(t) \right|_{T_S} \cong v_{outA}(t),$$ (2.11)

$$\left. v_{B0_{av}}(t) \right|_{T_S} \cong v_{outB}(t).$$ (2.12)

Functions $v_{outA}(t)$ and $v_{outB}(t)$ represent the desired inverter output voltages for each half-bridge that can be expressed as:

$$v_{outA}(t) = +\frac{\hat{V}}{2}\cos(\omega_o t),$$ (2.13)

$$v_{outB}(t) = -\frac{\hat{V}}{2}\cos(\omega_o t).$$ (2.14)

Now, the duty cycle functions $D_A(t)$ and $D_B(t)$ can be evaluated from (2.9) to (2.14), respectively:

$$D_A(t) = \frac{1}{2} + \frac{1}{2}\frac{\hat{V}/2}{(V_d/2)}\cos(\omega_o t) = \frac{1}{2} + \frac{1}{2}m_I\cos(\omega_o t),$$ (2.15)

$$D_A(t) = \frac{1}{2} - \frac{1}{2}\frac{\hat{V}/2}{(V_d/2)}\cos(\omega_o t) = \frac{1}{2} - \frac{1}{2}m_I\cos(\omega_o t),$$ (2.16)

where $m_I = \hat{V}/V_d$ is modulation index.

An auxiliary triangular carrier signal $v_{carr}(t)$ needs to be introduced in order to transform the duty cycle functions $D_A(t)$ and $D_B(t)$ into a switching function $d_A(t)$ and $d_B(t)$. Fig. 3(a) and 3(b) show the triangular carrier signal, and both switching functions signal, respectively. The switching functions $d_A(t)$ and $d_B(t)$ were obtained by a comparison of duty cycle functions $D_A(t)$ and $D_B(t)$ with $v_{carr}(t)$ as follows:

$$d_A = \begin{cases} 1, & D_A(t) \geq v_{carr}(t), \\ 0, & D_A(t) < v_{carr}(t), \end{cases} \qquad d_B = \begin{cases} 1, & D_B(t) \geq v_{carr}(t), \\ 0, & D_A(t) < v_{carr}(t). \end{cases}$$ (2.17)

The above-described procedure enables the generation of the triggering pulses in electrical circuits for all the semiconductor switches in the inverter. When referring to Fig. 4, the comparators (*comp*) compare the duty cycle functions $D_A(t)$ and $D_B(t)$ with triangular carrier signal (v_{carr}) and the signals $d_A(t)$, $d_a(t)$, $d_B(t)$ and $d_b(t)$ are obtained according to (2.5), (2.6) and (2.17).
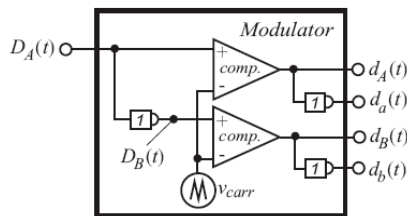
Figure 4: *Modulator block-scheme.*

The switching signals generated according to (2.17) can be considered to be periodic signals on the time interval $[0, T_s]$. When they are provided to the inverter switches, the three-level voltage (as shown in Fig. 2(a) and Fig. 3, respectively) appears at the inverter output:

$$v_{AB}(t) = \begin{cases} +V_d, & d_A(t) = 1, d_B(t) = 0, D_A(t) \geq D_B(t), \\ 0, & d_A(t) = 0, d_B(t) = 0 \vee d_A(t) = 1, d_B(t) = 1, \\ -V_d, & d_A(t) = 0, d_B(t) = 0, D_A(t) < D_B(t). \end{cases} \quad (2.18)$$

It is well known that any periodic signal of period T_s can be expanded into a trigonometric Fourier series form:

$$d_A(t) = \frac{a_0}{2} + \sum_{n=1}^{\infty} (a_n \cos(n\omega_T t) + b_n \sin(n\omega_T t)), \quad (2.19)$$

where ω_T is the frequency of the triangular carrier signal ($\omega_T = 2\pi/T_s$), and the coefficients a_0, a_n and b_n form a set of real numbers associated uniquely with the function $d_A(t)$:

$$a_0 = \frac{2}{T_s} \int_{t_0}^{t_0+T_s} d_A(t) dt,$$

$$a_n = \frac{2}{T_s} \int_{t_0}^{t_0+T_s} d_A(t) \cos(n\omega_T t) dt, \quad (2.20)$$

$$b_n = \frac{2}{T_s} \int_{t_0}^{t_0+T_s} d_A(t) \sin(n\omega_T t) dt.$$

Each term $a_n \cos(n\omega_T t) + b_n \sin(n\omega_T t)$ defines one harmonic function that occurs at integer multiples of the triangular carrier signal frequency $n\omega_T$. According to the signal waveform of the pulse train shown in Fig. 3(a), the Fourier coefficients can now be evaluated as:

$$d_A(t) = \begin{cases} 1, & t_0 - \dfrac{D_A(t)T_s}{2} \leq t \leq t_0 + \dfrac{D_A(t)T_s}{2}, \\ 0, & elsewhere. \end{cases} \quad (2.21)$$

In order to simplify the coefficient's calculation, the initial time $t_0 = 0$ is chosen, so the coefficient a_0 is:

$$a_0 = \frac{2}{T_s} \int_{-\frac{D_A(t)T_s}{2}}^{+\frac{D_A(t)T_s}{2}} 1\, dt = 2D_A(t) \quad (2.22)$$

Coefficients a_n are also calculated from (2.20):

$$a_0 = \frac{2}{T_s} \int_{-\frac{D_A(t)T_s}{2}}^{+\frac{D_A(t)T_s}{2}} 1\cos(n\omega_T t)\, dt = \frac{2}{\pi} \frac{\sin(n\pi D_A(t))}{n} \quad (2.23)$$

and all coefficient b_n are equal to 0. According to (2.19) the Fourier series of $d_A(t)$ is:

$$d_A(t) = D_A(t) + \frac{2}{\pi} \sum_{n=1}^{\infty} \frac{\sin(n\pi D_A(t))}{n} \tag{2.24}$$

and also for the switching function $d_B(t)$:

$$d_B(t) = D_B(t) + \frac{2}{\pi} \sum_{n=1}^{\infty} \frac{\sin(n\pi D_A(t))}{n} \tag{2.25}$$

2.2 The Output Voltage Spectrum Calculation

The output voltage $v_{AB}(t)$ can be constructed simply by subtracting outputs $v_{A0}(t)$ and $v_{B0}(t)$. In practice, when the load is connected between terminals A and B, the voltage difference $v_{AB}(t)$ appears on it. When (2.8) is subtracted from (2.7) it follows to:

$$v_{AB}(t) = (d_A(t) - d_B(t))D_d \tag{2.26}$$

The switching functions $d_A(t)$ and $d_B(t)$ can be expanded by the Fourier series in (2.24) and (2.25), respectively, and after applying (2.26) the inverter output voltage $v_{AB}(t)$ can be expressed by using the Bessel function as described in *[7], [8], [10]*:

$$v_{AB}(t) = m_l V_d \cos(\omega_o t) + \frac{4V_d}{\pi} \sum_{n=1}^{\infty} \frac{1}{n} \Big[$$

$$\cos(\frac{n\pi}{2}) J_1(\alpha) \big[\cos((n\omega_T + \omega_o)t) + \cos((n\omega_T - \omega_o)t) \big]$$

$$-\cos(\frac{n\pi}{2}) J_3(\alpha) \big[\cos((n\omega_T + 3\omega_o)t) + \cos((n\omega_T - 3\omega_o)t) \big] \tag{2.27}$$

$$\cos(\frac{n\pi}{2}) J_5(\alpha) \big[\cos((n\omega_T + 5\omega_o)t) + \cos((n\omega_T - 5\omega_o)t) \big] \dots \; \Big]$$

where $\alpha = nm_l\pi/2$. The structure of the spectral line's appearance is evident from (2.27). The SPWM signal $v_{AB}(t)$ has a fundamental component that appears at the frequency ω_o and, in addition to at the triangular carrier signal frequency $2n\omega_T$, also contains the sideband harmonics at frequencies $n\omega_T + k\omega_o$, $n = 1,2,3,...\infty$, $k = \pm1,\pm2,\pm3,...\infty$. Since the value of $\cos(n\pi/2)$ is zero for every odd n, the spectral lines only appear around even multiples of the carrier frequency $f_T = \omega_T/(2\pi)$, which is indicated in Tables 1 and 2, respectively. Fig. 2(b) shows the spectrum lines for the single-phase inverter's three-level output voltage for the $V_d = 330$ V and $m_l = 1$, line frequency $f_o = 50$ Hz and $f_T = 2$ kHz. From all the analyses above and the obtained results, the following conclusions can be made:

- The spectrum lines appear only for every even multiplier of f_T,
- The triangular carrier signal frequency $f_T = 2$ kHz is present in the half-bridge voltages ($v_{A0}(t)$ and $v_{B0}(t)$ not considered separately), but the synthesized inverter's output voltage $v_{AB}(t)$ switching frequency is doubled, so the first higher harmonic component appears next to the 4 kHz, and
- Filter components are needed at the inverter output to extract the first harmonic component at the fundamental frequency and reject the high switching frequency components of the output voltage $v_{AB(t)}$. The doubled switching frequency allows reduction of the size and weight of the filter components.

Table 1: *Spectral lines around the second multiplier of triangle carrier signal frequency $2f_T$.*

a_{21}	$\frac{4V_d}{\pi}\frac{1}{2}\cos(\frac{2\pi}{2})J_1(\frac{2\pi}{2}m_l)$	-63.4 V
a_{23}	$-\frac{4V_d}{\pi}\frac{1}{2}\cos(\frac{2\pi}{2})J_3(\frac{2\pi}{2}m_l)$	74.3 V
a_{25}	$-\frac{4V_d}{\pi}\frac{1}{2}\cos(\frac{2\pi}{2})J_5(\frac{2\pi}{2}m_l)$	-11.6 V

Table 2: *Spectral lines around the second multiplier of triangle carrier signal frequency $4f_T$.*

a_{41}	$\frac{4V_d}{\pi}\frac{1}{4}\cos(\frac{4\pi}{2})J_1(\frac{4\pi}{2}m_l)$	-23.7 V
a_{43}	$-\frac{4V_d}{\pi}\frac{1}{4}\cos(\frac{4\pi}{2})J_3(\frac{4\pi}{2}m_l)$	-3.2 V
a_{45}	$-\frac{4V_d}{\pi}\frac{1}{4}\cos(\frac{4\pi}{2})J_5(\frac{4\pi}{2}m_l)$	41.4 V

3   OVER-MODULATION PHENOMENON IN A SINGLE-PHASE INVERTER

The first harmonic magnitude for three-level output voltage (see (2.27)) is defined by $a_f = m_l V_d$ and has a position at the angular frequency ω_o (or frequency f_o). Obviously, the maximum magnitude of the first harmonic equals V_d due to the range of $m_l \in (0,1)$. The first harmonic magnitude can be increased over V_d when over-modulation is applied, which means that the modulation index must exceed $m_l \in (0,1)$. With over-modulation, an increased magnitude of the first harmonic component is welcome in some applications but, as a consequence of this phenomenon, the additional low-frequency spectrum lines appear.
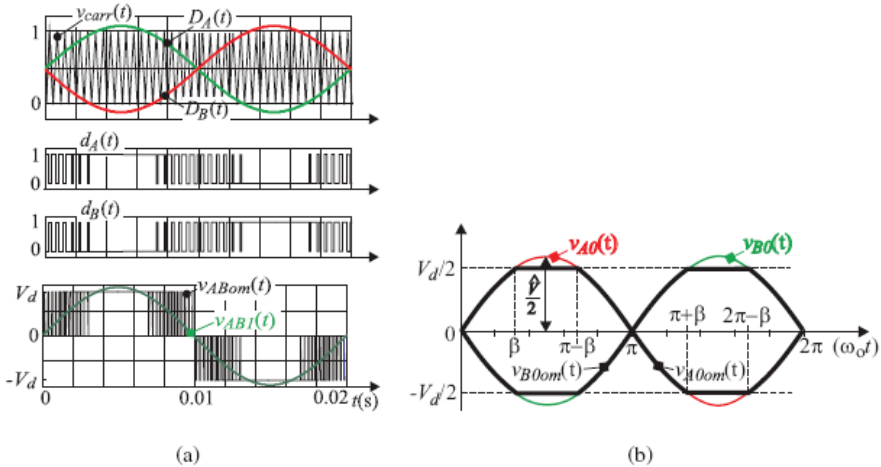
Figure 5: *Over-modulation procedure (m_l = 1.2): (a) Triangle carrier signal and duty cycle function $D_A(t)$, switching functions $d_A(t)$ and $d_B(t)$ waveforms. (b) Over-modulated desired half-bridge voltages $v_{A0om}(t)$ and $v_{B0om}(t)$.*

The three-level output voltage signal at the inverter output and over-modulation's influence on the frequency spectrum will be considered in the following subsections. Over-modulation appears when the duty cycle function $D_A(t)$ exceeds the magnitude of the high-frequency triangular carrier signal ($m_I > 1$). Fig. 5(a) shows a relationship between the triangular carrier signal and duty cycle function $D_A(t)$ and its influences on the switching functions $d_A(t)$ and $d_B(t)$ when a 20% over-modulation is applied, respectively.

3.1   The Duty Cycle Function Evaluation

Duty cycle functions can be evaluated in over-modulation as follows from (2.15) and (2.16) by applying $v_{A0om}(t)$ and $v_{B0om}(t)$ instead of $v_{A0}(t)$ exceeds $v_{B0}(t)$:

$$D_A(t) = \frac{t_A}{T_s} = \frac{1}{2} + \frac{1}{2}\frac{\hat{V}/2}{V_d/2}v_{A0om}(t) \tag{3.1}$$

$$D_B(t) = \frac{t_B}{T_s} = \frac{1}{2} + \frac{1}{2}\frac{\hat{V}/2}{V_d/2}v_{B0om}(t) \tag{3.2}$$

where of $v_{A0om}(t)$ and $v_{B0om}(t)$ are shown in Fig. 5(b) and are defined as follows:

$$v_{A0om}(t) = \begin{cases} \dfrac{\hat{V}}{2}\sin\omega_o t, & 0 \le \omega_o t < \beta, \\[2mm] +\dfrac{V_d}{2}, & \beta \le \omega_o t < (\pi - \beta), \\[2mm] \dfrac{\hat{V}}{2}\sin\omega_o t, & (\pi - \beta) \le \omega_o t < (\pi + \beta) \\[2mm] +\dfrac{V_d}{2}, & (\pi + \beta) \le \omega_o t < (2\pi - \beta) \\[2mm] \dfrac{\hat{V}}{2}\sin\omega_o t, & (2\pi - \beta) \le \omega_o t < 2\pi, \end{cases} \tag{3.3}$$

and

$$v_{B0om}(t) = \begin{cases} -\dfrac{\hat{V}}{2}\sin\omega_o t, & 0 \le \omega_o t < \beta, \\[2mm] -\dfrac{V_d}{2}, & \beta \le \omega_o t < (\pi - \beta), \\[2mm] -\dfrac{\hat{V}}{2}\sin\omega_o t, & (\pi - \beta) \le \omega_o t < (\pi + \beta) \\[2mm] +\dfrac{V_d}{2}, & (\pi + \beta) \le \omega_o t < (2\pi - \beta) \\[2mm] -\dfrac{\hat{V}}{2}\sin\omega_o t, & (2\pi - \beta) \le \omega_o t < 2\pi. \end{cases} \tag{3.4}$$

The voltages described by (3.3) and (3.4) can be expressed using Fourier series. The functions are odd, and due to this, the coefficients $a_n = 0$, so the voltages $v_{A0om}(t)$ and $v_{B0om}(t)$ are only

expressed by coefficients b_n, yielding:

$$v_{A0om}(t) = \sum_{k}^{\infty} b_k \sin(k\omega_o t),$$ (3.5)

$$v_{B0om}(t) = -\sum_{k}^{\infty} b_k \sin(k\omega_o t),$$ (3.6)

where $k = 1,3,5,...$ and the Fourier coefficients b_k can be evaluated from (3.3) by taking the symmetry of the signal during the half of the period:

$$b_k = \frac{2}{T} \int_{0}^{T/2} \left[f(\omega_o t) - f(-\omega_o t) \right] \sin(k\omega_o t) dt,$$ (3.7)

where $T = 2\pi/\omega_o$, so it follows:

$$b_k = \frac{2V_d}{\pi} \left[\frac{m_I}{2} \left[\frac{\sin[(k-1)\beta]}{(k-1)} - \frac{\sin[(k+1)\beta]}{(k+1)} \right] + \frac{1}{k} \cos(k\beta) dt \right],$$ (3.8)

where β is computed as follows from Fig. 5(b):

$$\beta = \arcsin\left(\frac{V_d}{\hat{V}} \right) = \arcsin\left(\frac{1}{m_I} \right)$$ (3.9)

Substituting (3.5) and (3.6) into (3.1) and (3.2), respectively, the duty cycle functions become:

$$D_A(t) = \frac{1}{2} + \frac{1}{V_d} \sum_{k}^{\infty} b_k \sin(k\omega_o t),$$

$$D_B(t) = \frac{1}{2} - \frac{1}{V_d} \sum_{k}^{\infty} b_k \sin(k\omega_o t),$$ (3.10)

3.2 The Over-Modulated Frequency Spectrum Calculation

The over-modulated output voltage can be evaluated from (2.26), (3.3) and (3.4):

$$v_{ABom}(t) = v_{A0om}(t) - v_{B0om}(t) = (d_A(t) - d_B(t))V_d$$ (3.11)

where the switching functions $d_A(t)$ and $d_B(t)$ can be evaluated by Fourier series as in (2.24) and (2.25), respectively and when combined with (3.10), the line to line voltage $v_{ABom}(t)$ can be expressed as:

$$v_{ABom}(t) = 2\underbrace{\left(\sum_{k}^{\infty} b_k \cos(k\omega_o t) \right)}_{LFSC} + HFSC,$$ (3.12)

where LFSC means "Low-Frequency Spectral Components" and HFSC "High-Frequency Spectral Components", which can be calculated as follows:

$$\text{HFSC} = \frac{4V_d}{\pi}\left(\sum_{n=1}^{\infty}\frac{1}{n}\cos\frac{n\pi}{2}\sin\left(\frac{n\pi}{V_d}\left(\sum_{k}^{\infty}b_k\cos(k\omega_o t)\right)\right)\sin n\omega_T t\right). \tag{3.13}$$

Eq. (3.12) consists of two parts: The first describes the low-frequency spectrum lines (next to the fundamental frequency ω_o), and the second describes the position and magnitudes of the high-frequency spectrum lines (next to the multipliers of triangle frequency ω_T). The over-modulation phenomenon is used in order to increase the first harmonic magnitude over the supply voltage when $\hat{V}_{AB1} \geq V_d$.

According to (3.8) and (3.12), the output voltage's low frequency harmonic components can be evaluated as follows:

$$\hat{V}_{ABk} = 2b_k = \frac{4V_d}{\pi}\left[\frac{m_I}{2}\left[\frac{\sin[(k-1)\beta]}{(k-1)} - \frac{\sin[(k+1)\beta]}{(k+1)}\right] + \frac{1}{k}\cos(k\beta)\right], \tag{3.14}$$

for the first, third, fifth and all odd spectral components, the (3.14) can be rewritten as (where in case of the first harmonic the division by zero can be avoided by replacing the function $\sin x = x$ for $m_I \gg$, or $\beta \ll$):

$$\hat{V}_{AB1} = \frac{4V_d}{\pi}\left[\frac{m_I}{2}\left[\beta - \frac{\sin(2\beta)}{2}\right] + \cos(\beta)\right], \tag{3.15}$$

$$\hat{V}_{AB3} = -\frac{4V_d}{\pi}\left[\frac{m_I}{2}\left[\frac{\sin(2\beta)}{2} - \frac{\sin(4\beta)}{4}\right] + \frac{1}{3}\cos(3\beta)\right], \tag{3.16}$$

$$\hat{V}_{AB5} = -\frac{4V_d}{\pi}\left[\frac{m_I}{2}\left[\frac{\sin(4\beta)}{4} - \frac{\sin(6\beta)}{6}\right] + \frac{1}{5}\cos(5\beta)\right]. \tag{3.16}$$
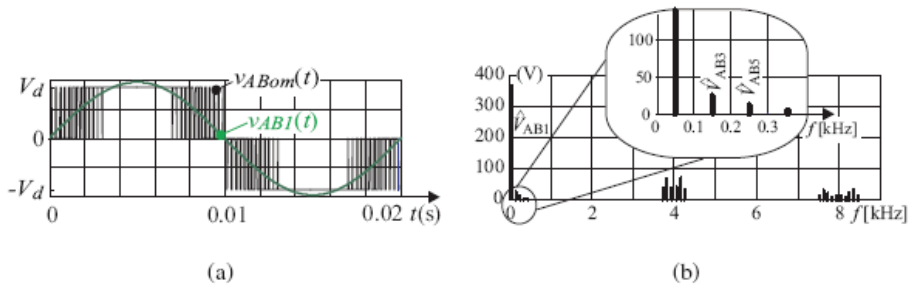
*Figure 6: (a) Over-modulated output voltage $v_{ABom}(t)$ and its first harmonic component $v_{AB1}(t)$.
(b) The low and high harmonic components spectrum lines.*

Fig. 6(a) shows the three-level output voltage $v_{AB}(t)$ for $V_d = 350$ V, $m_I = 1.2$, line frequency $f_o = 50$ Hz and $f_T = 2$ kHz, while its spectrum lines are presented in Fig. 6. From all the analyses above and the obtained results for spectrum evaluation the following conclusions can be made:

- The HFSC spectrum lines calculated by (3.13) appear only for every even multiplier of f_T,

- The LFSC spectrum lines calculated by (3.12) are zoom-out in Fig. 6, while the calculated values for the magnitude as well as the normalized values V_{ABkn} for the first, third and fifth harmonic components are given in Table 3 for the case of 20% over-modulation. The magnitude of first harmonic component $\hat{V}_{AB1}$ that exceeds the DC-voltage V_d by 10.4% was calculated by (3.15).

Table 3: Spectral lines around the second multiplier of triangle carrier signal frequency $4f_T$.

$\hat{V}_{AB1}$	$\dfrac{4V_d}{\pi}\left[\dfrac{m_I}{2}\left[\beta-\dfrac{\sin(2\beta)}{2}\right]+\cos(\beta)\right]$	386.6 V	V_{AB1n}	1.1046
$\hat{V}_{AB3}$	$-\dfrac{4V_d}{\pi}\left[\dfrac{m_I}{2}\left[\dfrac{\sin(2\beta)}{2}-\dfrac{\sin(4\beta)}{4}\right]+\dfrac{1}{3}\cos(3\beta)\right]$	-25.1 V	V_{AB3n}	0.0717
$\hat{V}_{AB5}$	$\dfrac{4V_d}{\pi}\left[\dfrac{m_I}{2}\left[\dfrac{\sin(4\beta)}{4}-\dfrac{\sin(6\beta)}{6}\right]+\dfrac{1}{5}\cos(5\beta)\right]$	-12.9 V	V_{AB5n}	0.0369

Fig. 7(a) shows the calculated first, second and third harmonic components versus modulation index changed from 0 to 2. When m_I exceeds 1, the magnitudes of harmonic components start to increase as follows from the presented over-modulation analysis.
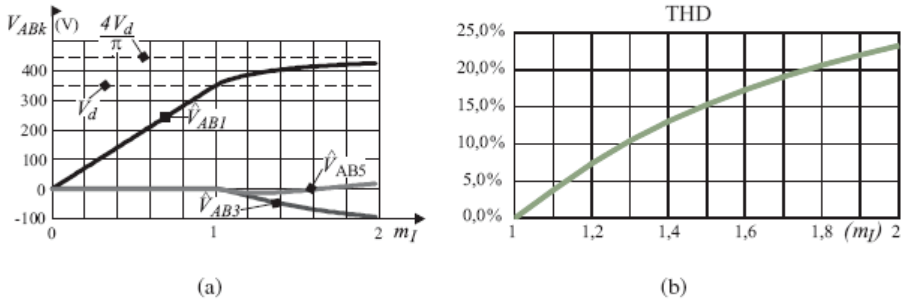
Figure 7: (a) First, third and fifth harmonic components versus modulation index $m_I \in (0,2)$. (b) THD versus modulation index $m_I \in (1,2)$.

To validate the presented procedure's correctness, a single-phase low-voltage (V_d = 20 V) inverter experimental set up based on the DRV8870DDAR integrated circuit was built in the laboratory. The described SPWM strategy was implemented using a Texas Instruments TMDSCNCD28335 control card that can be programmed in MATLAB SIMULINK and is ideal to use for initial evaluation and system prototyping. Output voltage over ohmic load was measured with a RIGOL DS2102A Digital storage oscilloscope. Fig. 8(a) presents the measured output voltage when the inverter operates in over-modulation with m_I = 1.2 while Fig. 8(b) shows its normalized frequency spectrum calculated by FFT in MATLAB. The obtained results show clearly that the normalized values for the first, third, and fifth harmonic components

match almost perfectly the predicted values calculated with the described procedure (see Table 3).
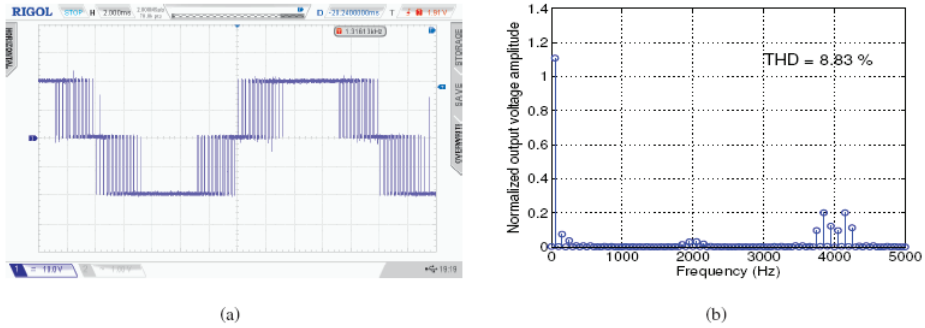
Figure 8: (a) Inverter output voltage at m_I = 1.2 and (b) Its frequency spectrum.

3.3 The Upper Limit Calculation

The upper limit is obtained when the modulation index m_I goes to infinity and, according to Fig. 5(b), the angle β goes to 0. The upper limit can be evaluated as follows:

$$\hat{V}_{ABk,\max} = \lim_{\beta\to\infty} \frac{4V_d}{\pi}\left[\frac{m_I}{2}\left[\frac{\sin[(k-1)\beta]}{(k-1)}-\frac{\sin[(k+1)\beta]}{(k+1)}\right]+\frac{1}{k}\cos(k\beta)\right] \quad (3.18)$$

and after calculation through a limit process:

$$\hat{V}_{ABk,\max} = \frac{4V_d}{\pi}\frac{1}{k} \quad (3.19)$$

It is evident from (3.19) that the upper limit for the first (fundamental, where k = 1) voltage harmonic component is:

$$\hat{V}_{ABk,\max} = \frac{4V_d}{\pi} \quad (3.20)$$

and is indicated as the upper limit line (i.e. at the square-wave output signal) in Fig. 7(a). The over-modulation operation of the inverter also has significant influence on the THD factor that is defined as:

$$THD = \frac{\sqrt{\sum_{k=2}^{n}\hat{V}_{ABk}^2}}{\hat{V}_{AB1}} \quad (3.21)$$

THD factor dependence on modulation index m_I is presented in Fig. 7(b). The maximum permissible THD factor is defined for different load types, so it is possible to set the necessary modulation index m_I which defines the first harmonic component magnitude $\hat{V}_{AB1}$ and, consequently from (3.15), the appropriate DC voltage V_d can be determined. In some special cases in which the available DC voltage supply V_d does not meet the requirements regarding the

magnitude of the output voltage $\hat{V}_{AB1}$ ($V_d < \hat{V}_{AB1} \leq \hat{V}_{AB1,\max}$), this over-modulation property allows us to omit the DC-DC boost converter in the power supply system.

4   CONCLUSION

In this paper, a straightforward, step-by-step SPWM frequency spectrum analysis has been presented for a single-phase inverter as an indispensable part of renewable energy source systems. The precise, analytical approach to SPWM signal analysis is rather unpopular among many engineers due to the relatively long and complicated procedure but, to understand these processes, it is necessary to take advantage of it. The additional reason that the analytical approach is not widely used in practice is due to the widespread usage of the MATLAB Software package. This program enables FFT numerical analysis of the PWM processes but, by using FFT, engineers do not gain an in-depth insight into the connections between the different quantities appearing in the formulas.

For three-level inverter output voltage, and over-modulation, principles of modulation algorithms have been developed here in a traditional analytical way. The electronic circuit of an SPWM modulator can be realized from the described algorithms by using new microcomputer technology and in the paper presented knowledge is also a good base for further investigation into SPWM switching strategies. The over-modulation phenomenon can help engineers to speculate using the inverter's parameters; for example, it can decrease the DC input voltage V_d and the output voltage will still have the necessary magnitude of the first harmonic component $\hat{V}_{AB1}$. The obtained results were experimentally verified in order to prove the procedure's correctness.

This analysis could be easily extended to three-phase inverters intended for electrical motor drive applications or grid-connected. And finally, the results of this analysis are also appropriate for further investigation of SPWM processes with respect to higher harmonic components' influence on losses for the different types of loads, as well as for filter design in the single-phase inverters used in UPS or grid-connected back-up systems.

References

[1]   **G. Wang, G. Konstantinou, C.D. Townsend, J. Pou, S. Vazquez, G.D. Demetriades, and V.G. Agelidis:** *A review of power electronics for grid connection of utility-scale battery energy storage systems*, IEEE Trans. Sustainable Energy, vol. 27 no. 4, pp. 1778-1790, Oct. 2016

[2]   **R. Theodorescu, M. Liserre, P. Rodríguez:** *Grid Converters for Photovoltaic and Wind Power Systems*, West Sussex: IEEE Press/John Wiley & Sons, Inc., 2011

[3]   **F. Mihalič and A. Hren:** Isolated bi-directional DC-DC converter, *Journal of Energy Technology*, vol. 3, no. 3, pp. 27-40, Aug. 2010

[4]   **H.S. Black:** *Modulation Theory*, New York: Van Nostrand Reinhold Company, 1953

[5]   **M. Odavic, M. Summer, P. Zanchetta, and J.C. Clare:** *A theoretical analysis of the harmonic content of PWM waveforms for multiplefrequency modulators, IEEE Trans. Power Electronics*, vol. 25, no. 1, pp. 131-141, Jan. 2010

[6]   **G. Fedele and D. Frascino:** *Spectral analysis of class of dc-ac PWM inverters by Kapteyn series,* IEEE Trans. Power Electronics, vol. 25, no. 4, pp. 839-849, April 2010

[7]   **N. Mohan, T.M. Undeland, W.P. Robbins:** *Power Electronics, Devices, Converter, Application and Design*, second ed., New York: John Wiley & Sons., 1995

[8]   **R.W. Ericson, D. Maksimovic:** *Fundamentals of Power Electronics*, Dordrecht: Kluwer Academic Publisher, 2001

[9]   **P. Wood:** *Switching Power Converters*, New York: Van Nostrand Reinhold Company, 1981

[10]   **D.G. Holmes, T.A. Lipo:** *Pulse Width Modulation for Power Converters: Principles and Practice*, New York: IEEE Press/John Wiley & Sons, Inc., 2003

[11]   **H.S. Patel and R.H. Hoft:** *Generalized technique of harmonic elimination and voltage control in thyristor inverters: Part I - Harmonic elimination*, IEEE Trans. Industry Applications, vol. IA-9, no. 3, pp. 310-317, May/Jun. 1973

[12]   **A. Alesina and M.G.B. Venturini:** *Solid-state power conversion: a Fourier analysis approach to generalised transformer synthesis*, IEEE Trans. Circuits Systems, vol. CAS-28, no. 11, pp. 319-330, April 1981

[13]   **J. Holtz:** *Pulsewidth modulation - A survey*, IEEE Trans. Industrial Electronics, vol. 39, no. 5, pp. 410-420, Oct. 1992

[14]   **V.G. Agelidis, A.I. Balouktsis, and C. Cossar:** *On attaining the multiple solutions of selective harmonic elimination PWM three-level waveforms through function minimization*, IEEE Trans. Industrial Electronics, vol. 55, no. 3, pp. 996-1004, Mar. 2008

[15]   **S.A. Saleh, C.R. Molonay, and M. Azzizur Rahman:** *Analysis and development of wavelet modulation for three-phase voltage source inverters*, IEEE Trans. Ind. Electron., vol. 58, no. 8, pp. 3330-3348, Aug. 2011

[16]   **A. Alesina and M.G.B. Venturini**: *Analysis and design of optimum-amplitude nine-switch direct ac-ac converter*, IEEE Trans. Power Electronics, vol. 4, no. 1, pp. 101-112, Jan. 1989

[17]   **M. Milanovič and B. Dobaj:** *Unity input displacement factor correction principle for direct ac to ac matrix converters based on modulation strategy*, IEEE Trans. Circuits Systems I, vol. 4, no. 2, pp. 221-230, Feb. 2000

[18]   **H. Koizumi, K. Kurokawa, and S. Mori**: *Analysis of class D inverter with irregular driving patterns*, IEEE Trans. Circuits Syst. I, vol. 53, no. 3, pp. 677-687, Mar. 2006

[19]   **K.M. Cho, W.S. Oh, Y.T. Kim, and H.J. Kim:** *A new switching strategy for pulse width modulation (PWM) power converters*, IEEE Trans. Ind. Electron., vol. 54, no. 1, pp. 330-337, Feb. 2007

[20]   **S.R. Bowes and D. Holliday:** *Optimal regular-sampled pwm inverter control techniques*, IEEE Trans. Ind. Electron., vol. 54, no. 3, pp. 1547-1559, Jun. 2007

[21]   **Q. Li, P. Wolfs:** *A review of the single phase photovoltaic module integrated converter topologies with three different DC link configurations*, IEEE Trans. Power Electron., vol. 23, no. 3, pp. 1320-1332, May 2008

[22]   **R.H. Green and J.T. Boys:** *Implementation of pulsewidth modulated inverter modulation strategies*, IEEE Trans. Ind, Appl., vol. IA-18, no. 2, pp. 138-145, Mar./Apr. 1983

[23] **R.O. Caceres and I. Barbi:** *A boost dc-ac converter: analysis, design, and experimentation*, IEEE Trans. Power Electron., vol. 14, no. 1, pp. 134-141, Jan. 1999

[24] **Z. Song and D.V. Sarwate:** *The frequency spectrum of pulse width modulated signals*, Signal Processing, vol. 83, no. 10, pp. 2227-2258, 2003

Nomenclature

(Symbols)	(Symbol meaning)
b_k	Fourier series coefficients
β	cross-section angle in the over-modulation
$d_A(t)$	switching function
$D_A(t)$	duty-cycle function
$J_i(\alpha)$	Bessel functions
m_I	modulation index
ω_T	triangular carrier signal frequency
ω_o	fundamental output voltage frequency
FFT	fast Fourier transformation
HFSC	high-frequency spectral components
LFSC	low-frequency spectral components
SPWM	sinusoidal pulse-width modulation
THD	total harmonic distortion
UPS	uninterruptible power supply

Journal of
Energy
Technology

HYDRAULIC TRANSIENT CONTROL OF NEW AND REFURBISHED KAPLAN TURBINE HYDROPOWER SCHEMES IN SLOVENIA

BLAŽENJE PREHODNIH POJAVOV V SLOVENSKIH NOVIH IN OBNOVLJENIH HIDROELEKTRARNAH S KAPLANOVIMI TURBINAMI

Jernej Mazij[℞], Anton Bergant[1]

Abstract

As a natural resource, water is abundant in Slovenia, and its exploitation for electricity generation has a long history. The construction of Kaplan-type turbines is preferred due to topographical and environmental conditions. Water hammer control strategies, including issues of axial hydraulic thrust calculations, are presented in this paper. The case studies include new and refurbished hydropower plants located on all three major river basins in Slovenia.

Povzetek

Slovenija ima dolgo zgodovino izrabe vodnih virov za proizvodnjo električne energije. Zaradi topografskih in ekoloških omejitev je gradnja hidroenergetskih objektov z visokimi pregradami omejena. V Sloveniji prevladujejo pretočne hidroelektrarne z vgrajenimi kaplanovimi turbinami.

℞ Corresponding author: Jernej Mazij, BSc, Litostroj Power d.o.o., Litostrojska 50, 1000 Ljubljana, Slovenia, jernej.mazij@litostrojpower.eu

[1] Anton Bergant, PhD, Litostroj Power d.o.o., Litostrojska 50, 1000 Ljubljana, Slovenia, anton.bergant@litostrojpower.eu

V tem prispevku so predstavljene strategije nadzora negativnih posledic prehodnih pojavov, vključno s problemi pri izračunih aksialnih hidravličnih sil. Praktični pristop je predstavljen na novih in prenovljenih hidroelektrarnah, ki se nahajajo na povodjih rek Save, Drave in Soče.

1   INTRODUCTION

Together with forests, water is the only true natural resource in abundant supply in Slovenia. With an annual quantity of 17,000 m³ of water per capita, the country is ranked third in Europe, after Switzerland and Norway, *[1]*. Two water regions divide the country; the Danube River (Black Sea) and the Adriatic seawater region. There are three major river basins (catchment areas): Drava, Sava, and Soča. They are characterized by a combination of nival and nival-pluvial regimes. The gross hydropower potential is estimated at 19,440 GWh/year. Thus far, 45% of the total technically available potential has been exploited: 4,115 GWh/year. Hydropower plants generate approximately 30% of the total installed capacity.

Conditions for the construction of high-head hydropower schemes or conventional reservoirs with high dams are not favourable. Most of the corresponding potential sites are in environmentally sensitive areas or sites where construction would not be economically feasible.

Electricity generation in Slovenia using hydropower started at the end of the 19th century with the first turbine installed in Škofja Loka, *[2]*. Construction of the Završnica hydropower plant in 1914 and the Fala hydropower plant in 1918 marked a turning point in terms of the electrification of the country.

Major developments were made after 1945 with the return of to Primorska region to Slovenia with its hydropower plants on the Soča River and the systematization of electricity distribution. In the 1960s, the construction of hydropower plants on the Sava and Drava Rivers began, to meet basic demands for electricity and continued through the 1970s. The post-independence period saw interconnection of the Slovenian power grid to the common European network. Construction of the chain of hydropower plants on the lower Sava River began, as did the start of refurbishment of existing facilities.

Regarding the river basins, the Sava River basin is the largest and represents more than 50% of the total country area but is the least utilized in terms of hydropower, with a total installed capacity of 230 MW. Completion of the chain on the lower Sava River is underway, and the start of the procedure for the design of the middle Sava River chain with 10 hydropower plants is foreseen. Unfortunately, political, economic, and environmental issues are hindering the project.

The Drava River basin is the most important and the most developed, with an installed capacity of 600 MW. A comprehensive refurbishment programme has been completed with the replacement of all obsolete electromechanical equipment. The Drava is a border river, and the operating regime of the chain must be co-ordinated with the operation of the chain on the Austrian side for a daily run-of-river storage regime.

The Soča River basin is ideal for hydropower production due to its high annual rainfall in the southern Alpine mountains. Three major hydropower plants have a total capacity of 142 MW and a pump-storage plant at Avče (the only one in Slovenia) completes the Soča River basin utilization with additional 180 MW capacity.

There is also the Mura River, but it is not currently being exploited for hydroelectric production due to environmental restrictions. The river has a nival regime of discharge as the waters are fed from the central Alpine mountains, and maximum annual discharges occur in late spring. This is favourable in comparison with other catchment areas which lack water during the summer. The possible foreseen installed capacity is 158 MW based on the principle of flow-of-the river, which has less influence on natural habitats, *[1].*

2   HYDRAULIC TRANSIENTS

General issues related to hydraulic transients have already been presented, *[3, 4]*. These issues include transient operating regimes, transient control, and modern approaches to transient modelling.

Specific transient issues relating to Kaplan turbines the will be covered in this paper are:

- relatively short inlet and outlet conduits and the usage of rigid column water hammer theory,

- check for water column separation under the turbine head cover,

- calculation and measurement of axial hydraulic thrust,

- installation of a surge tank for a low-head Kaplan development.

Modelling will be performed using commercial computer packages *[5, 6].*

The EPFL SIMSEN commercial software package, *[5]*, is based on modular structure, composed of objects, in which each object represents a specific network element. Hydraulic elements are modelled as RLC electrical circuits according to the impedance method, *[7]*. Momentum and mass conservation equations provide the basis for an equivalent electrical circuit modelling.

The transient behaviour of a hydraulic machine can be modelled using the steady-state characteristics (hill chart). Turbine characteristics are given in forms of unit speed, unit discharge and unit torque (n_{11}, Q_{11}, M_{11}) for different guide vane openings A_0 and for different runner blade angles (blade pitch angle) β are used.

Due to the traditionally relatively short inlet and outlet conduits (length of the conduit is of the same order as the cross-sectional dimensions) and complex cross-sectional shapes, the rigid column water hammer theory is the basis for the MISI TRANK software package, *[6]*. The rigid water hammer is described by the one-dimensional Bernoulli equation for unsteady flow, which is solved simultaneously with the dynamic equations of the turbine unit rotating masses, taking into account the turbine characteristics. In addition to unit discharge and unit torque, the unit axial hydraulic thrust characteristics (F_{a11}) are implemented in the turbine model.

2.1   Water column separation and axial hydraulic thrust

Transient regimes must be controlled in such a way that the operation of the turbine is safe and reliable. One of the most severe transient regimes is the emergency shut-down triggered by the over-speed device, which is set to operate in the event of an excessive speed rise, *[8]*.

Attention should be paid to reverse water hammer, which can occur in hydropower plants with long outlet conduits. Water column separation can occur under the turbine head cover and the draft tube inlet during the closing of the turbine (guide vanes and runner blades). Two approaches are used in the estimation of the potential danger of full column separation, *[9]*.

Turbine head cover pressure criterion. Based on model measurements, the absolute pressure under the turbine head cover is calculated. Pressure is measured at several locations in the space between the guide vanes and runner blades. The pressure under the turbine head cover is then calculated using measured axial hydraulic thrust characteristics. The computed absolute pressure should be larger than the vapour pressure $p_a > p_{vp}$.

Axial hydraulic thrust criterion. The potential danger of full column separation and turbine unit lifting during transient events are estimated using the measured model axial hydraulic thrust characteristics. Full column separation under the head cover and subsequent cavity collapse induces large axial hydraulic thrust acting upwards. If the absolute value of the acting hydraulic thrust is greater than the total weight of the rotating parts of the unit, then the unit may be lifted from the thrust bearings causing structural damage. The following expression is valid:

$$\left| F^-_{a,\max} \right| = \min \left\{ \left| F^-_{ad} \right|, W_u \right\}$$

(2. 1)

The damaging axial hydraulic thrust is calculated by the following equation in which the full water column separation under the head cover is assumed to occur:

$$F^-_{ad} = -\rho g \, \frac{\pi D^2}{4} \left(1 - \frac{d^2}{D^2} \right) \left(10 - \frac{Z_{twl}}{900} \right) + \rho g \, \frac{\pi D^2}{4} \left(H_s - \Delta H_i \right)$$

(2)

The dynamic head is calculated with the following equation:

$$\Delta H_i = \frac{Q_{sc} G_d}{g t_{sc}}$$

(2. 2)

The installation of air valves has limited influence on the application of the above criterion and cannot prevent damaging reverse water hammer.

Eight run-of-the-river hydropower plants form a chain on the Slovenian part of the Drava River extending from the Austrian to the Croatian border. Over the last twenty years, seven HPP have been fully refurbished and upgraded. These include Fala HPP (1991), Dravograd HPP (1997), Mariborski otok HPP (1997), Vuzenica HPP (1997), Ožbalt HPP (2004), Vuhred HPP (2004), and Zlatoličje HPP (2012). A total of twenty Kaplan units were replaced with a new runner design with larger diameters (+5%) increasing the discharge capacity in the existing flow-passages by about 25-30%.

Zlatoličje HPP is designed as a channel-type power plant. It is the largest Kaplan type turbine in Slovenia and generates more than a fifth of all the electric power generated by its parent company DEM (Dravske Elektrarne Maribor). Constructed in 1966, the two units made use of 33-m head at a threshold capacity of 136 MW (160 MW after refurbishment in 2011). The plant is connected to a 17.2-km long trapezoidal profile inlet channel, see Figure 1. The outlet channel is 6.2 km long and joins the Drava River at Ptuj Lake, the largest artificial lake in Slovenia and the headwater level of the Formin HPP, the last hydropower plant on the Drava river.

Each of the two units is equipped with a pressure-regulating valve (PRV) comprised of five vertical vanes connected via a rod to a servomotor and controlled by the turbine governor. During transient operating regime, the PRV is designed to completely attenuate free surface waves in the inlet and outlet channels. The continuous measurements of the channel water levels at the turbine inlet and outlet have indicated that water level oscillations in the channels are small and within the prescribed limits during transient regimes. The dimensions of the inlet conduit, scroll casing, and the draft tube are expressed as geometric characteristics. The polar moment of generator inertia is $I = 3.375 \times 10^6$ kgm^2.

Figure 1: *Zlatoličje HPP (photo www.dem.si.)*

Emergency shut-down of the Kaplan turbine from 75 MW output or 94% of full-load is considered to be one of the most severe normal operating regimes with respect to large transient pressure heads, turbine rotational speed and surges in open channel.

The turbine is disconnected from the electrical grid followed by the complete closure of the wicket gates while the runner blades open to their fully open position (Figure 2(a)). The PRV blades first open to about 90% opening synchronously with the wicket gate closure and then start to close at a very slow rate to its fully closed position. The PRV linear full-stroke closing time is $t_{c,\ PRV}$ = 1200 s. The continuous measurement of the channel water levels at the turbine inlet and outlet indicates that water level oscillations in the open channel are small and within the prescribed limits during the transient event. Figure 2(b) shows measured headwater level variations (Z_{HWL}) during the period of the turbine closure. During this period of the transient operating regime, the pressure regulating valve completely attenuates free surface waves in the inlet channel. This is practically true for the oscillations in the outlet channel too (Figure 2(d)). Therefore, the constant water levels at the turbine inlet and the turbine outlet are assumed in water hammer calculations. Analysis of free surface waves in the inlet and outlet channel is beyond the scope of this paper.
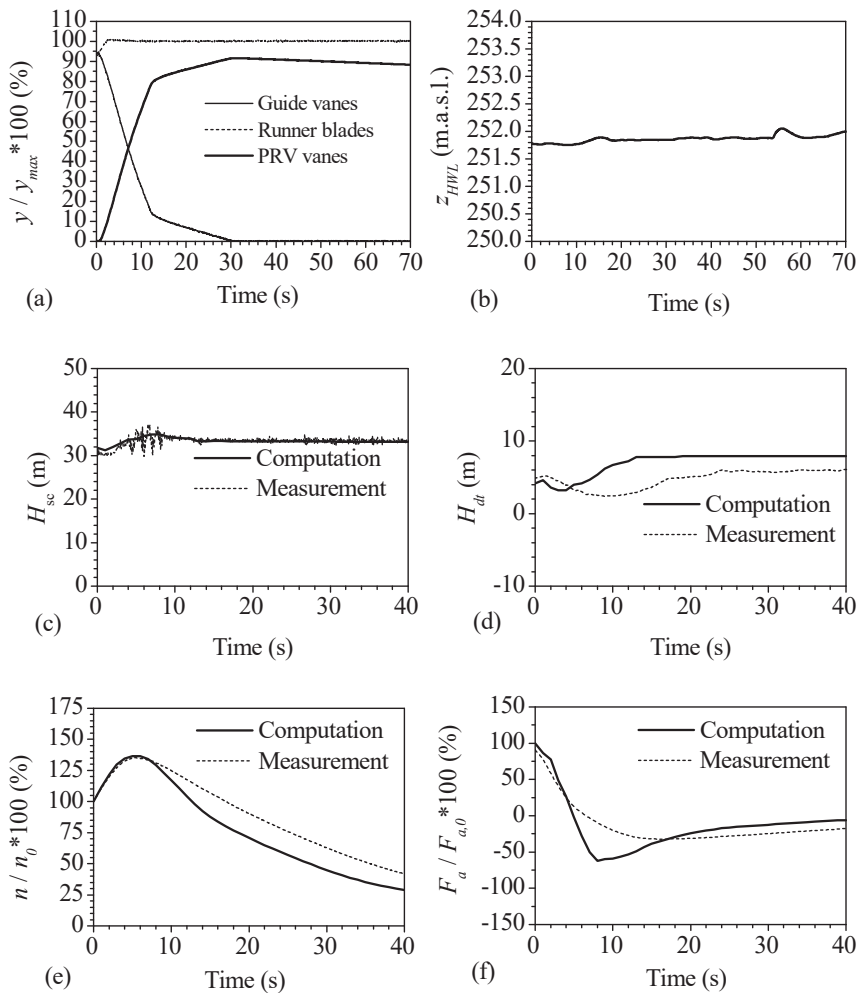
Figure 2: *Emergency shut-down in Zlatoličje HPP (P = 75 MW): Guide vane and runner blade servomotor strokes (a), headwater level at the turbine inlet (b), scroll case (c) draft tube heads(d), unit rotational speed (e) and axial hydraulic thrust (f)*

The assumed flow-passage system used for rigid water hammer analysis is comprised of relatively short inlet scroll case and outlet (draft tube) conduits. Figure 2(c-f) shows results of rigid column water hammer analysis for the considered emergency shut-down of the unit. The agreement between the computed and measured maximum rotational speed rise of 35% and 36.5%, respectively, (Figure 2(e); n_0 = 125 min^{-1}) is good. The computed maximum momentary scroll case pressure head (H_{sc}) of 35 m practically coincides with the averaged measured one (Figure 2(c); there is a reasonable agreement between the calculated and measured draft tube pressure head too (Figure 2(d)). The maximum scroll case pressure head and the maximum speed rise are within the prescribed limits. The calculated and the measured maximum momentary negative axial hydraulic thrusts (absolute values) of 3500 kN and 1600 kN, respectively are less than the

permissible thrust $|F^-_{a,max}|$ = 5370 kN (Figure 2(f); $F_{a,0}$ = 5680 kN). There is a large discrepancy between the magnitudes of the negative axial hydraulic thrust. The maximum calculated axial hydraulic thrust is based on model measurements. It is difficult to measure hydraulic quantities in the model at smaller wicket gate openings (large uncertainties), in particular at an increased rotational speed of the turbine. There is also a large uncertainty in the measured axial hydraulic force on the prototype. However, the general trace of calculated and measured axial hydraulic thrust is similar.

4   CASE STUDY 2: KRŠKO HYDROPOWER PLANT

Construction on the lower Sava river reach is currently one of the largest infrastructure projects in Slovenia. Krško HPP is the fourth in a chain of six planned run-of-the-river hydropower plants. Upstream projects include Vrhovo HPP (1993), Boštanj HPP (2006), and Arto-Blanca HPP (2010). On the downstream side, Brežice HPP has been recently put into operation, and Mokrice HPP is under design review. Three Kaplan units with a total installed capacity of 39 MW are in a powerhouse constructed on the right side of the river bank (looking downstream), see Figure 3. Limited construction space, inaccessibility, the vicinity of the main road and the railway with deep excavations due to locally heavily fractured dolomite rock hindered construction in comparison to the other stages on the chain, *[10]*.

Figure 3: Krško HPP (photo Litostroj Power archive)

In an effort to lower construction and maintenance costs, the mechanical and civil engineering designs are as uniform as possible. After completion, all hydropower plants in the chain will operate fully automated and unmanned. The polar moment of generator inertia is I = 700 × 10⁶

Emergency shut-down of the unit 11.7 MW output is observed. Figure 4 shows results of rigid column water hammer analysis for the considered emergency shutdown.

The agreement between the computed and measured maximum rotational speed rise of 23% and 26.7%, respectively, (Figure 4(b); n_0 = 100 min^{-1}) is good. The same can be said for the maximum scroll case pressure; the calculated value is 14.1 m, and the measured is 14.2 m (Figure 4(c)). The maximum scroll case pressure head and the maximum speed rise are within the prescribed limits.

The calculated and the measured maximum momentary negative axial hydraulic thrusts (absolute values) of 1354 kN and 641 kN, respectively, are less than the permissible thrust | $F^-_{a,max}$ | = 1943 kN (Figure 4(d)). The general trace of calculated and measured axial hydraulic thrusts is similar.
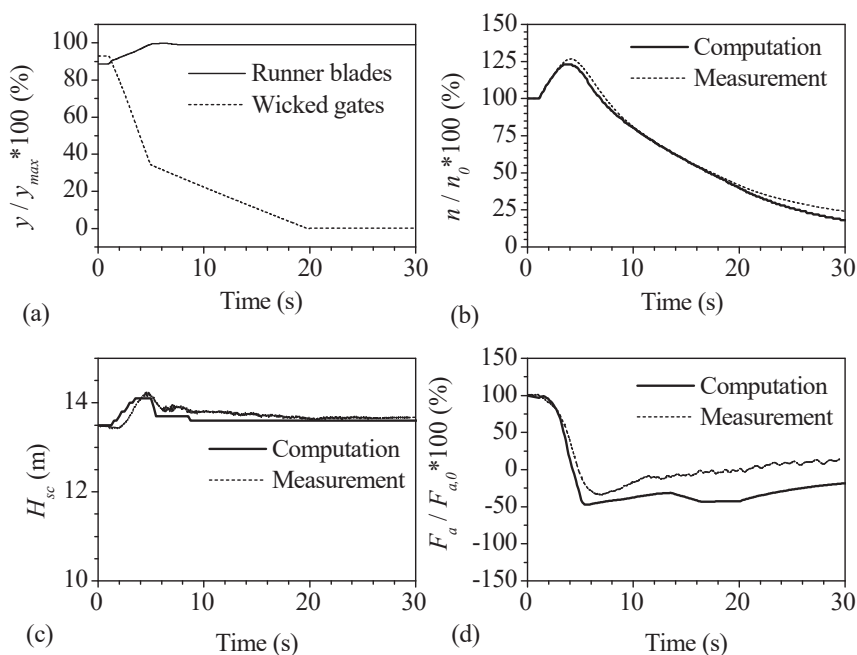
Figure 4: Emergency shut-down in Krško HPP (P = 11.7 MW): Guide vane and runner blade servomotor strokes (a), unit rotational speed (b), scroll case pressure (c) and axial hydraulic thrust (d).

5   CASE STUDY 3: PLAVE II HYDROPOWER PLANT

The design of Plave II HPP on the Soča River basin was based on exploiting the available hydro potential and infrastructure of the existing Plave I HPP, built prior to WWII. Intakes for both HPPs are located at the Ajba dam. While the Plave I HPP uses a free-surface water underground diversion channel, Plave II HPP has a low-pressure diversion tunnel connected at the end to an expansion chamber. The tunnel is lined with prefabricated concrete elements. The complete

length of the tunnel is 6 km with a diameter of 6.4 m and runs parallel to the Plave I HPP channel. The TBM method for tunnel construction was used for the first time in Slovenia. The expansion chamber (tunnel) connects the low-pressure tunnel to a double-cylinder surge tank, each of 26 m diameter. The low-pressure tunnel continues to the power station as a penstock in two sections divided by a gate chamber. Two vertical Kaplan turbines, each of 20.5 MW capacity, are installed in the powerhouse; see Figure 5.

Operation of both Plave I and Plave II HPP is fully unmanned and remotely operated from the control centre.

Due to the long tunnel with a surge tank and relatively long penstock, an elastic column water hammer model has been used, *[5]*. A simplified and detailed model of the surge tank will be presented, and results compared to measured values. Attention will be given to penstock pressure, rotational speed and surge tank water levels during emergency shut-down. Figure 6(a) presents the basic or simplified model of the flow-passage. Two surge tanks are replaced in the model with a single equivalent surge tank of 37 m diameter. The value of the surge tank intake losses is k_{in} = 0.00125 s^2/m^5 and outtake losses k_{out} = 0.00078 s^2/m^5. The design of the surge tank and orifice was tested in a hydraulic research laboratory.

Figure 6(b) presents a more detailed model of the flow-passage system. Two surge tanks are included as well as the connecting pipe from the low-pressure tunnel.
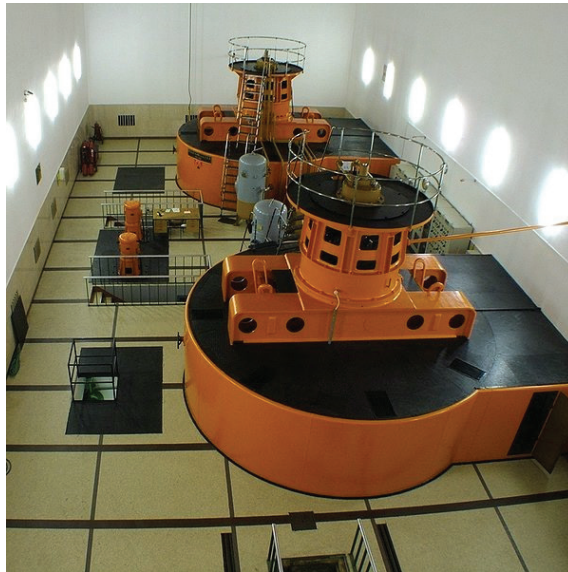
Figure 5: Plave II HPP machine hall (photo www.seng.si)

As seen from the results presented in Figure 7, the main difference between the models is in the result for the penstock pressure; 38 m for the simplified model and 44 m for the detailed model. The difference can be attributed to the inertia of the water in the connecting pipe between the low-pressure tunnel to the penstock. A minor difference is present for the rotational speed (219 min^{-1} vs. 225 min^{-1}), while there is no difference in the maximum surge

tank water level (109.6 m.a.s.l.). A comparison of the measured values confirms the detailed model.
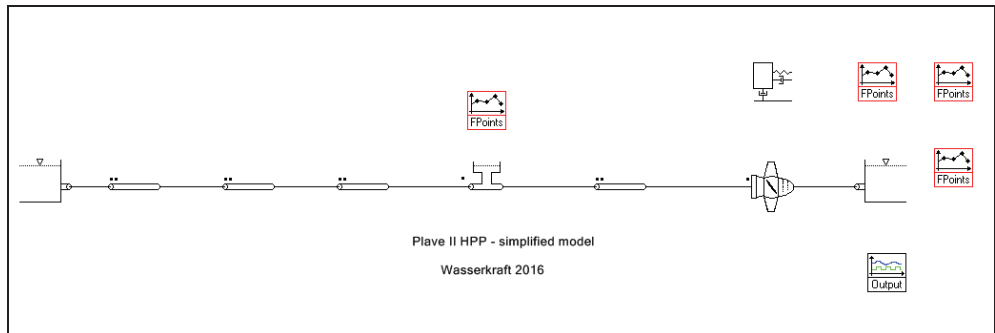
(a)
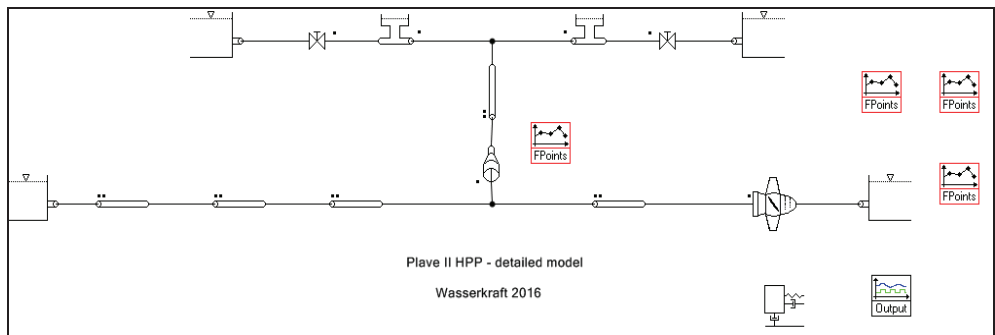
(b)

Figure 6: *Plave II HPP computational model*
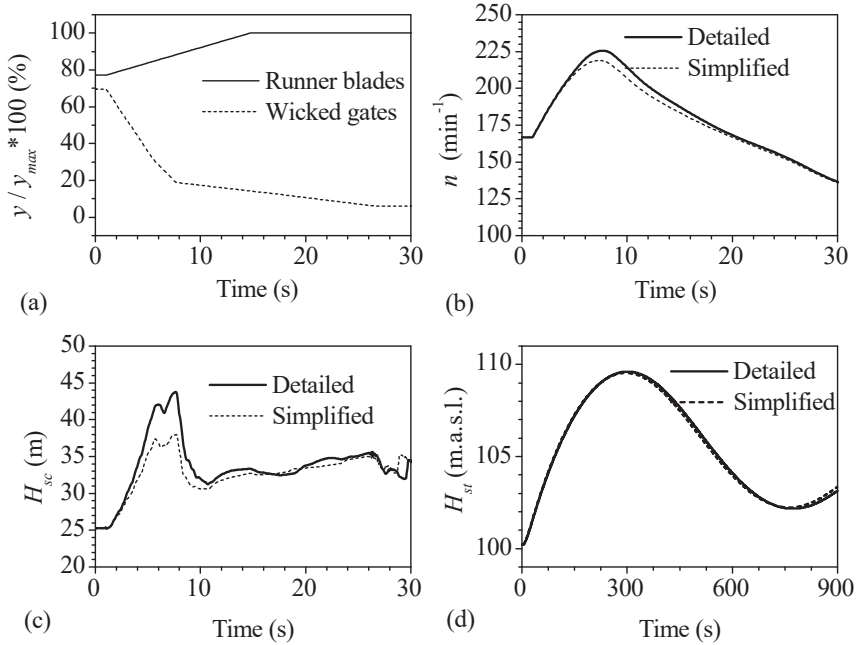
Figure 7: *Emergency shutdown in Plave II HPP: Guide vane and runner blade servomotor strokes (a), unit rotational speed (b), penstock pressure (c) and surge tank water level (d).*

Complete tabulated measured results are not available (different measuring chains in the surge tank chamber and in the machine hall); therefore, a direct comparison is not presented. Figure 8(a) shows measured results for penstock pressure (p_{sp}) and rotational speed (n). Wicket gates and runner blades servomotor strokes are labelled y_2 and y_3, respectively. Figure 8(b) shows results for the surge tank water level oscillations over a prolonged interval during commissioning testing. The emergency shut-down that is taken into consideration is labelled M55.

Note: Figures 8(a) and 8(b) are taken directly from the original commissioning report, [10]; therefore, the text is in its original (Slovenian) language.

Figure 8a: *Emergency shutdown in Plave II HPP (P = 18 MW): Measured results for guide vane and runner blade servomotor strokes, penstock pressure, and rotational speed*
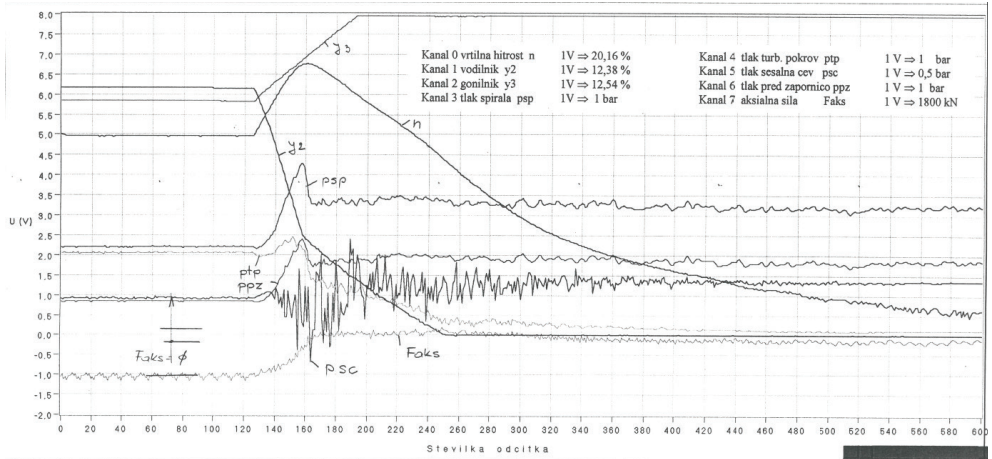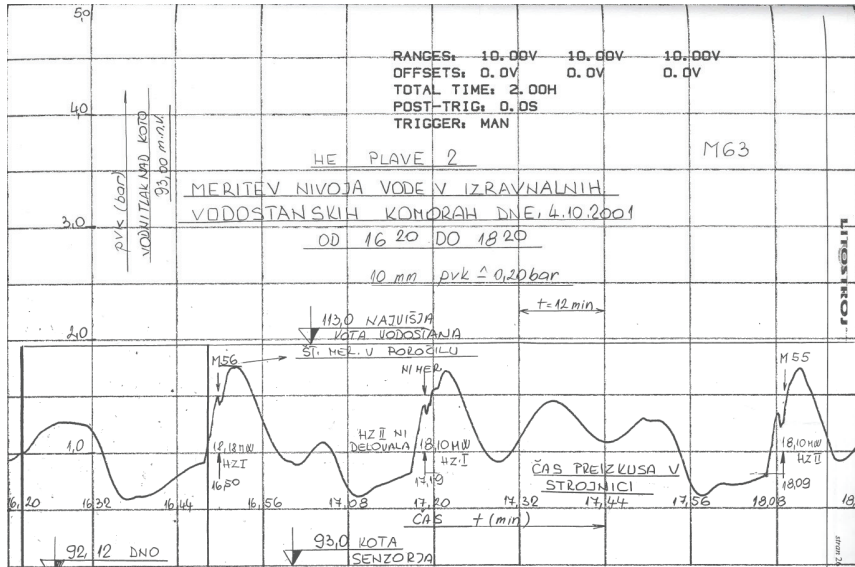

Figure 8b: *Emergency shutdown in Plave II HPP (P = 18 MW): Measured results for surge tank water level oscillations*

6   CONCLUSIONS

This paper presents three typical case studies of water hammer control strategies of Kaplan turbine hydropower plants in Slovenia. Particular design approaches, water hammer control strategies, and critical flow regimes that may induce unacceptable water hammer loads are outlined. Hydroelectric power plants with Kaplan turbines are traditionally comprised of relatively short inlet and outlet conduits; therefore, the rigid column water hammer theory is used for these cases. For systems with long penstocks, elastic column water hammer theory should be used.

Acknowledgments

References

[1]   **Kryžanovsky et al**.: *Hydro potential and development opportunities in Slovenia*, Hydropower & Dams 5, 41-46, 2008

[2]   **I. Tršelič**: *Large hydropower plants in Slovenia*, Journal of Energy Technology 7, 21-32, 2014

[3]   **J. Mazij, A. Bergant**: *Hydraulic transient analysis – Issues related to refurbished and new hydropower schemes with complex water conveyance systems*, Wasserkraftanlagen 2014, Vienna, 2014

[4]   **J. Mazij, A. Bergant, D. Dolenc, J. Gale**: *From general design to commissioning – hydraulic transient analysis in case of high-head hydropower plant Toro III*, Hydro 2013, Innsbruck, 2013

[5]   **EPFL** Computer package SISMEN version 3.0.1, Lausanne, Switzerland 2015

[6]   **MISI** Computer package TRANK, Moscow, Russia 1984

[7]   **C. Nicolet**: *Hydroacoustic modelling and numerical simulation of unsteady operation of hydroelectric systems*, Dissertation*, EPFL, Lausanne, Switzerland 2007

[8]   **J. Fašalek, S. *Rakčević*: *Air valves and control of the Kaplan turbine during transients*, IAHR 1986*, Montreal, 1986

[9]   **A. Bergant, E. Sijamhodžić:** *Waterhammer control in Kaplan turbine hydroelectric power plants*, 8th International Conference on Pressure Surges 2000, The Hague, 2000

[10]   **A. Širca et al**.: *Construction of the Krško HPP on the lower Sava river*, Gradbeni vestnik 61, 70-76, 2016

[11]   **Litostroj Power**: *Commissioning report Plave II HPP*, Ljubljana, Slovenia 2001

Nomenclature

(Symbols)	(Symbol meaning)
D	runner diameter
d	turbine shaft diameter
F_a	axial hydraulic thrust
F_{ad}^-	damaging axial hydraulic thrust acting upwards
$F_{ad,max}^-$	maximum axial hydraulic thrust acting upwards
G_d	geometric characteristics of the draft tube
G_u	geometric characteristics of the inlet conduit and the scroll-casing
g	gravitational acceleration
H	pressure head
H_s	suction head
H_{dt}	draft tube head
H_{sc}	scroll case pressure
ΔH_i	dynamic head
I	polar moment of inertia
K	surge tank head losses (intake, outake)
n	turbine rotational speed
P	turbine output
p	pressure
Q	discharge
Q_{sc}	discharge at an assumed water column separation
t_{sc}	closing time from discharge Q_{sc} to $Q = 0$ m³/s
y	servomotor (guide vanes/runner blades) stroke
W_u	weight of the unit rotating parts
Z_{hwl}	headwater level
Z_{twl}	tailwater level
ρ	mass density

THE CALCULATION OF HIGH-PRESSURE VISCOSITY FOR REFRIGERANT MIXTURES

IZRAČUN VISKOZNOSTI PRI VISOKIH TLAKIH ZA ZMESI HLADIL

Jurij Avsec[ℜ], Urška Novosel[1]

Abstract

This paper features a mathematical model for computing the viscosity in the fluid domain for a hydrofluorocarbon mixture with the help of statistical thermodynamics. The viscosity pf HFC-134a (1,1,1,2-Tetrafluoroethane) and HFC-125 (Pentafluoroethane) mixtures was calculated as an example of hydrofluorocarbon mixtures. To calculate the thermodynamic properties of a real fluid, the models were applied based on the Lennard-Jones intermolecular potential. The analytical results obtained via statistical thermodynamics are compared with the experimental data and show relatively good agreement.

Povzetek

V članku je prikazan matematični model izračuna viskoznosti v plinastem področju za mešanico fluoroogljikovodikov s pomočjo statistične termodinamike. V predstavljenem članku smo izračunali viskoznost za zmes hladil HFC-134a (1,1,1,2-tetrafluoroetane) in HFC-125 (Pentafluoroetane) kot primer fluoriranih ogljikovodikov. Za izračun termodinamičnih lastnosti realne tekočine so bili uporabljeni modeli na podlagi Lennard-Jonesovega intermolekularnega potenciala. Analitični rezultati, pridobljeni s statistično mehaniko, so primerjani z eksperimentalnimi podatki in kažejo razmeroma dobro ujemanje.

ℜ Corresponding author: Corresponding author: Prof. Jurij Avsec, Ph. D., Tel.: +386-7-620-2217, Fax: +386-2-620-2222, Mailing address: Hočevarjev trg 1, 8270 Krško, Slovenia, E-mail address: jurij.avsec@um.si

[1] University of Maribor, Faculty of Energy Technology, Laboratory for Thermomechanics, Applied Thermal Energy Technologies and Nanotechnologies, Hočevarjev trg 1, SI-8270 Krško, Slovenia

1   INTRODUCTION

The computation of thermo-mechanical properties in the high-pressure range is vital for a large number of fluids that are essential to energy technology. Some great, even insurmountable problems remain in identifying analytical expressions for the transport characteristics of fluids at high pressures. Using super-computers and the methods of molecular dynamics, it is possible to follow each molecule in the system of particles. One drawback of numerical methods, however, is that analytical records of functions are unfortunately lost.

For more than half of century, chlorofluorocarbons (CFCs) have been used as working fluids in refrigeration, heat pump and air conditioning applications. These compounds are very stable, non-toxic and non-flammable and, therefore are regarded as safe refrigerants. For several decades chlorine-fluorine-hydrocarbons were considered harmless refrigerants. Most CFCs have been replaced by hydrofluorocarbons (HFCs) which have a similar molecular structure but do not contain chlorine atoms. For example, one of the most important CFCs, R12, has been already replaced by 1,1,1,2-tetrafluoroethane (R134a) in several applications. Refrigerants 134a and R125 are alternative refrigerants, which are suitable as substitutes for R22 and R502.

2   CALCULATION OF VISCOSITY BY STATISTICAL MECHANICS

Accurate knowledge of the nonequilibrium or transport properties of pure gases and liquids is essential for the optimum design of different items of chemical process plants, for the determination of intermolecular potential energy functions, and for the development of accurate theories of transport properties in dense fluids. Transport coefficients describe the process of relaxation to equilibrium from a state perturbed by the application of temperature, pressure, density, velocity, or composition gradients. The theoretical description of these phenomena constitutes that part of nonequilibrium statistical mechanics known as kinetic theory. From the semi-classical kinetic theory for polyatomic fluids the coefficients of thermal conductivity, shear viscosity and bulk viscosity can be expressed:

$$\lambda = \frac{2k^2T}{3m}[A,A], \ \eta = \frac{1}{10}kT[B,B], \ \kappa_s = kT[\Gamma,\Gamma] \tag{2.1}$$

where A, B and Γ are complex vector, tensor and the scalar functions, *[1,2,3]*. The detailed description of the physical origin of bulk viscosity is explained in the literature, *[2]*. It arises in dense polyatomic gases and liquids. The transport properties for pure gases are represented as sums of terms for the temperature-dependent dilute-gas contributions and terms for the temperature- and density-dependent residual contributions. Contributions for the critical enhancement are not included in these background functions. From the Boltzmann equation, for mono-atomic dilute gases, transport properties not far from the Maxwellian can be calculated, *[1-3]*. This means that transport phenomena are treated with small temperature or velocity gradients of the molecules. On this basis, the dynamic viscosity for single-component gas can be expressed:

$$\eta_0 = \frac{5kT}{8\Omega^{(2,2)}} \left(1 + \frac{3}{49} \left(\frac{\Omega^{(2,3)}}{\Omega^{(2,2)}} - \frac{7}{2} \right)^2 \right) \tag{2.2}$$

where, and $\Omega(l,s)$ is the transport collision integral. With the Lennard-Jones intermolecular potential, it is almost impossible to obtain collision integrals analytically. Because of the difficulty of calculating these integrals, their values are usually taken from published tables. To make computerized calculations more convenient and to improve on the accuracy obtainable by linear interpolation of the tables., the empirical formulation of Neufeld [5] et al. was used, obtained on the basis of numerical simulations and interpolation procedure.

$$\Omega^{(l,s)^*} = \frac{A}{T^{*B}} + \frac{C}{exp\left(DT^*\right)} + \frac{E}{exp\left(FT^*\right)} + \frac{G}{exp\left(HT^*\right)} + RT^{*B} sin(ST^{*W} - P) \tag{2.3}$$

This equation contains 12 adjustable parameters and is developed for 16 collision integrals. The dilute gas viscosity is obtained from kinetic theory assuming that a Lennard-Jones (LJ) potential applies, and using the expression:

$$\eta_0(T) = 26.69579 \cdot 10^{-1} \frac{\sqrt{MT}}{\Omega^{(2,2)^*}\sigma^2}, \tag{2.4}$$

where η is in Pa s, M is the molecular mass in gmol-1, T is in K, $\Omega(2,2)$ is a collision integral and σ is the Lennard-Jones parameter. In this paper, the Chung-Lee-Starling model (CLS) will be presented, *[6]*. Equations for the viscosity are developed based on kinetic gas theories and correlated with the experimental data. The low-pressure transport properties are extended to fluids at high densities by introducing empirically correlated, density dependent functions. These correlations use acentric factor ω, dimensionless dipole moment μr and an empirically determined association parameters to characterize the molecular structure effect of polyatomic molecules κ, the polar effect and the hydrogen bonding effect. In this paper, new constants for fluids are determined.

The dilute gas dynamic viscosity for the CLS model is written as:

$$\eta_0(T) = 26.69579 \cdot 10^{-1} \frac{\sqrt{MT}}{\Omega^{(2,2)^*}\sigma^2} F_c \tag{2.5}$$

The factor Fc has been empirically found to be [6]:

$$F_c = 1 - 0.2756\omega + 0.059035\mu_r^4 + \kappa \tag{2.6}$$

where ω is the acentric factor, μ_r relative dipole moment and κ is a correction factor for hydrogen-bonding effect of associating substances such as alcohols, ethers, acids, and water.

For dense fluids, Eq. (5) is extended to account for the effects of temperature and pressure by developing an empirically correlated function of density and temperature as shown below:

$$\eta = \eta_k + \eta_p \tag{2.7}$$

$$\eta_k = \eta_0 \left(\frac{1}{G_2} + A_6 Y \right) \tag{2.8}$$

$$\eta_p = \left[36.344 \cdot 10^{-6} - (MT_c)^5 / V_C^{2/3}\right] A_7 Y^2 G_2 \, exp(\, A_8 + A_9 / T^* + A_{10} / T^{*2}\,) \tag{2.8}$$

$$Y = \rho V_c / 6 \,, G_1 = \frac{1.0 - 0.5Y}{(1.0 - Y)^3} \tag{2.9}$$

$$T_c = \frac{1.2593\epsilon}{k_B}, V_c = (0.809\sigma(A))^3 \tag{2.10}$$

$$G_2 = \frac{\{A_1(1 - exp(-A_4 Y)) + A_2 G_1 \, exp(A_5 Y) + A_3 G_1\}}{(A_1 A_4 + A_2 + A_3)} \tag{2.11}$$

The constants A1-A10 are linear functions of the acentric factor, the reduced dipole moment, and the association factor

$$A_i = a_0(i) + a_1(i)\omega + a_2(i)\mu_r^4 + a_3(i)\kappa \,, i=1,10 \tag{2.12}$$

where the coefficients a_0, a_1, a_2, and a_3 are presented in the work of Chung at al., *[6]*.

For the determination of viscosity for fluid mixtures, a purely analytical model has been used, *[2]*. According to this theory, the viscosity of dense fluid mixtures containing N components can be written in the form:

$$\eta = -\frac{\begin{vmatrix} H_{11} & \cdots & H_{1N} & \psi_1 \\ \vdots & & \vdots & \vdots \\ H_{N1} & & H_{NN} & \psi_N \\ \psi_1 & & \psi_N & 0 \end{vmatrix}}{\begin{vmatrix} H_{11} & \cdots & H_{1N} \\ \vdots & & \vdots \\ H_{N1} & \cdots & H_{NN} \end{vmatrix}} \tag{2.13}$$

$$H_{ii} = \frac{\psi_i^2}{\eta_i} + \sum_{\substack{j=1 \\ j \neq i}}^{N} \frac{\psi_i \psi_j}{2\eta_{ij} A_{ij}^*} \frac{M_i M_j}{(M_i + M_j)^2} \left(\frac{20}{3} + \frac{4M_j}{M_i} A_{ij}^* \right) \tag{2.14}$$

$$H_{ij}(j \neq i) = -\frac{\psi_i \psi_j}{2\eta_{ij} A_{ij}^*} \frac{M_i M_j}{(M_i + M_j)^2} \left(\frac{20}{3} - 4A_{ij}^* \right) \tag{2.15}$$

where ρ is the molar density, ψ_i and ψ_j are mole fractions of species I and j, and M_i and M_j are their molecular masses. A_{ij}^* is a weak function of intermolecular potential for i-j interactions. The symbol η_i represents the viscosity of pure component i, and η_{ij} represents the viscosity of i-j interaction. We have developed the new equation for η_{ij}:

$$\eta_{ij} = \sqrt{\eta_i \eta_j} \tag{2.16}$$

3   RESULTS AND DISCUSSION

Figures 1-11 show the deviation of the results for ternary mixture R125+R134a in the real gas region between the analytical computation (CLS-Chung-Lee-Starling model) and experimental results, *[7-9]*. Table 1 shows the most important data for analytical calculation. The results for all transport properties obtained with the CLS model show relatively good agreement.

Table 1: *The important constants for analytical calculation for R125 and R-134a*

	R-134a	R-125
ε (J)	410.04E-23	337.678E-23
σ (m)	4.76E-10	5.005E-10
ω (-)	0.32684	0.3061
μ_r (-)	0.15	0.6
κ (-)	0	0
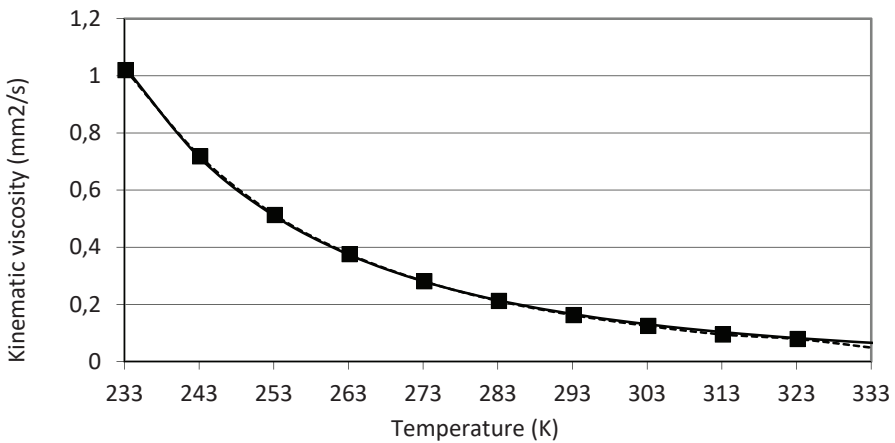
Figure 1: Kinenatic viscosity for R125 in saturated gas region
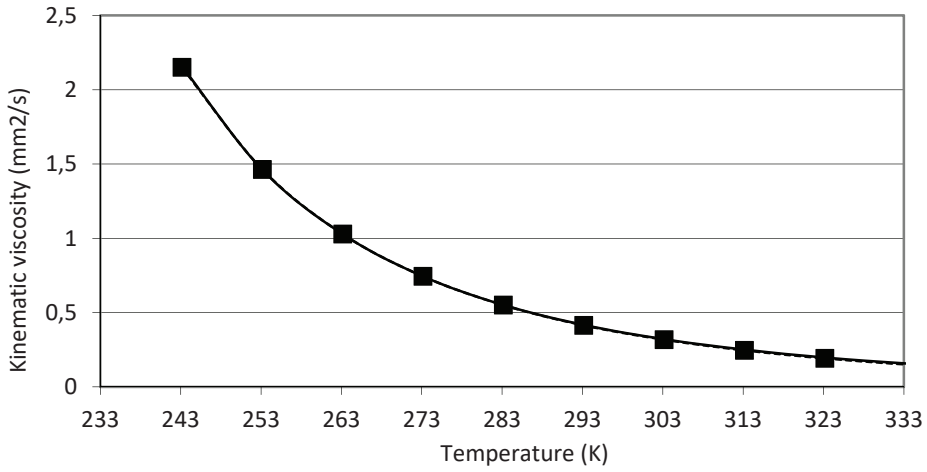
Figure 2: Kinenatic viscosity for R134a in saturated gas region
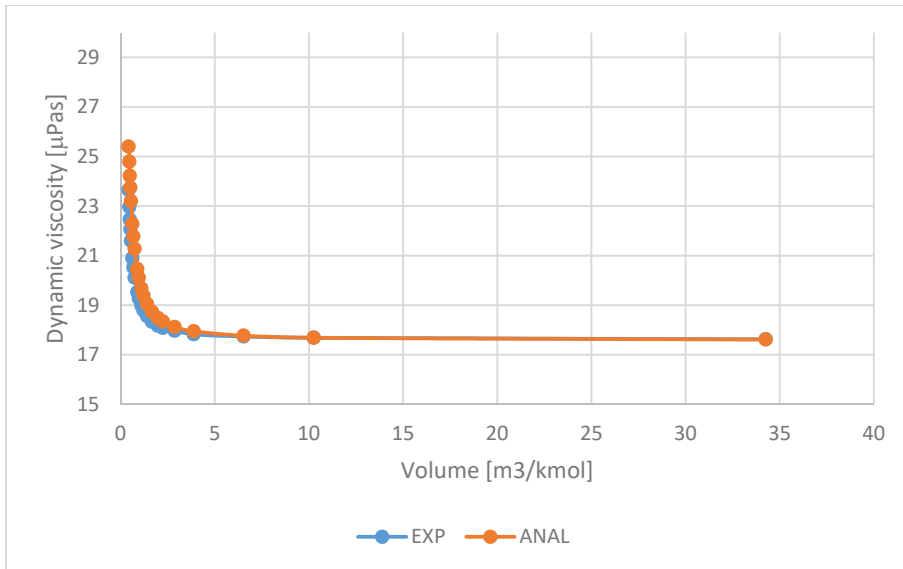
Figure 3: *Viscosity for mixture of R125+R134a at 423 K and 75.1% of R125*
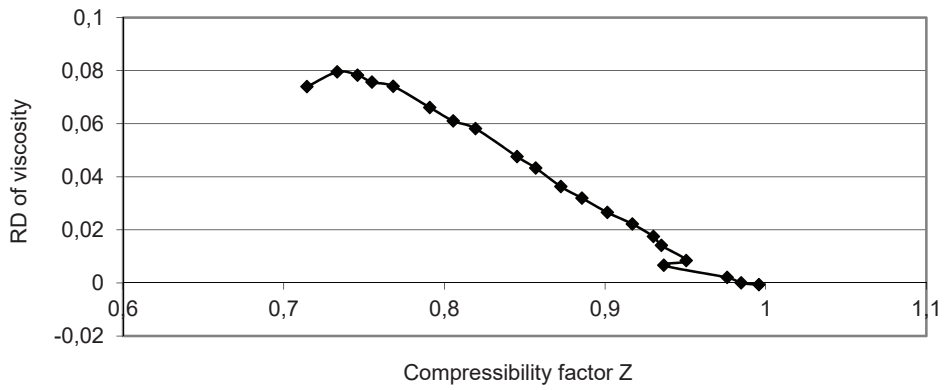
Figure 4: Compressibility factor for mixture of R125+R134a at 423 K and 75.1% of R125
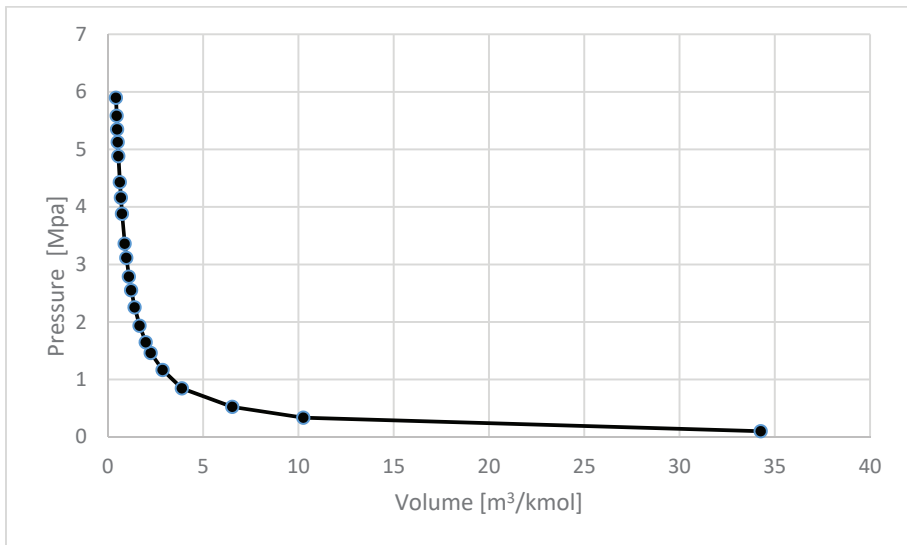
Figure 5: Pressure-volume diagram for mixture of R125+R134a at 423 K and 75.1% of R125
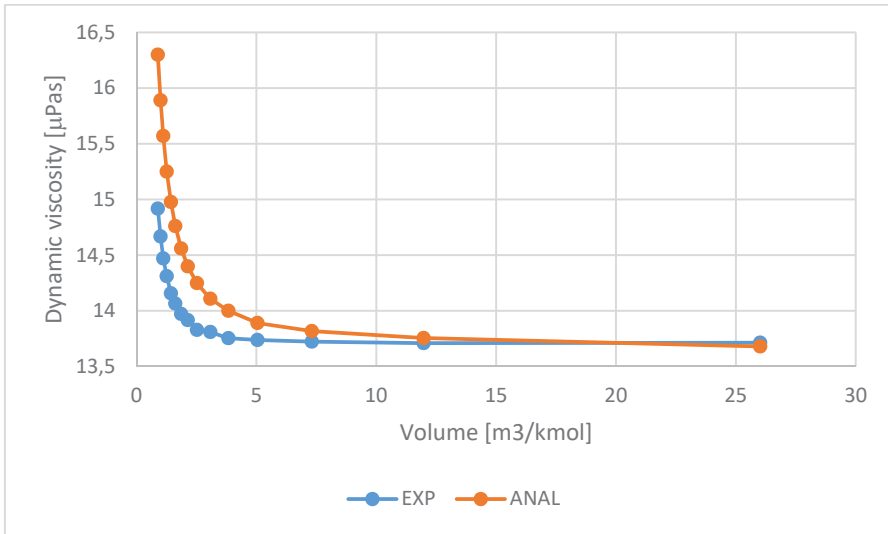
Figure 6: *Viscosity for mixture of R125+R134a at 323 K and 75.1% of R125*

T=323 K, 75.1%R125+24.9%R134a
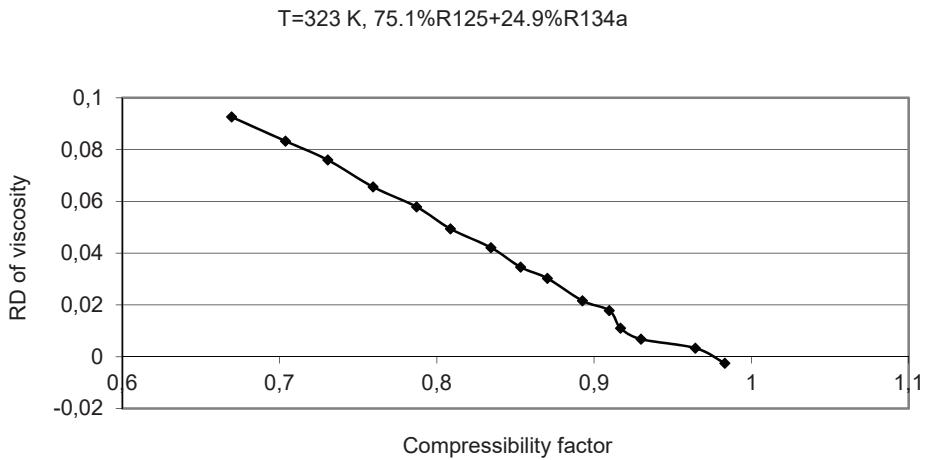
Figure 7: *Compressibility factor for mixture of R125+R134a at 323 K and 75.1% of R125*
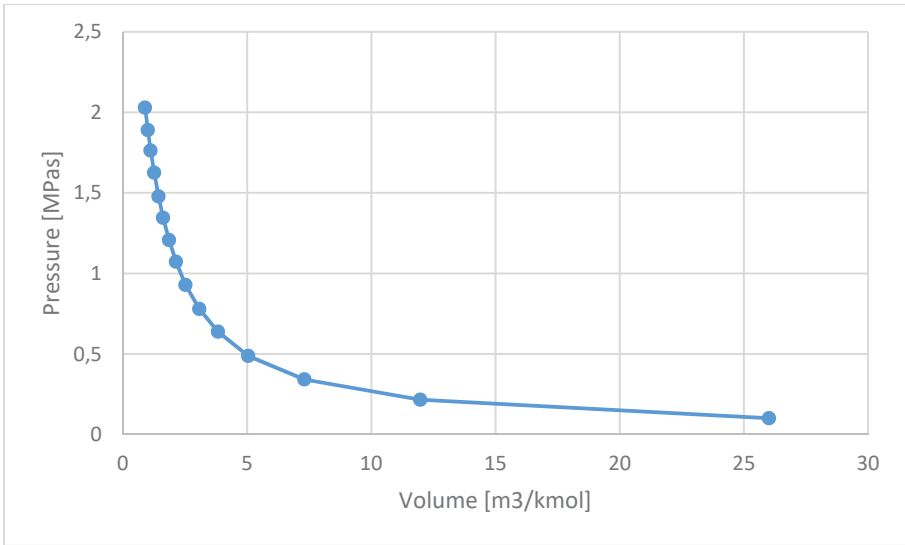
Figure 8: Pressure-volume diagram for mixture of R125+R134a at 423 K and 75.1% of R125
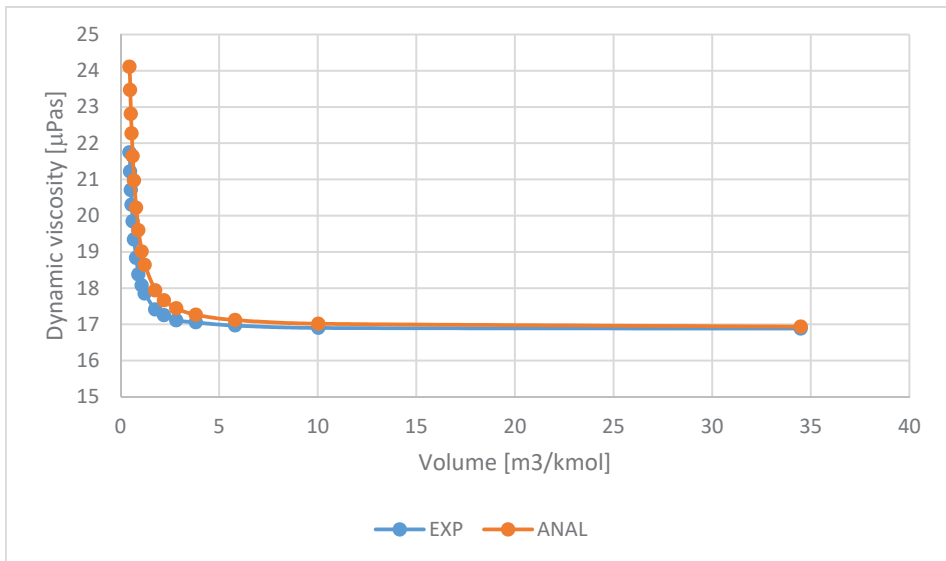
Figure 9: Viscosity for mixture of R125+R134a at 423 K and 75.1% of R125 and 25.1% of R125

T=423 K, 25.08%R125+74.92%R134a
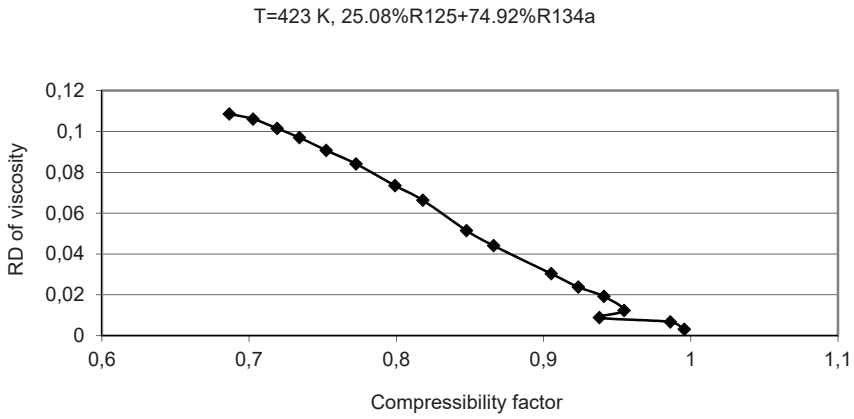
Figure 10: *Compressibility factor for mixture of R125+R134a at 423 K and 25.1% of R125*
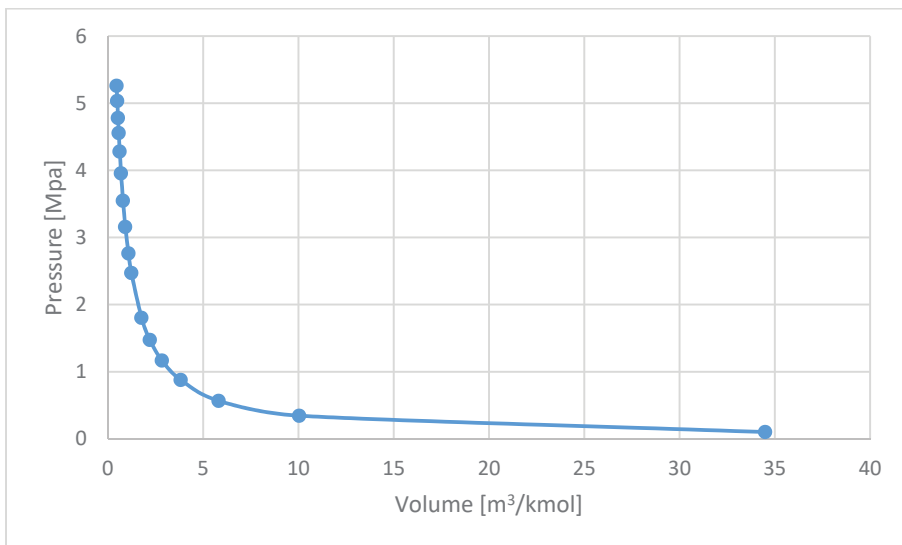
Figure 11: *Compressibility factor for mixture of R125+R134a at 423 K and 25.1% of R125*

References

[1**]** **J. Millat, J.H. Dymond**: *C.A. Nieto de Castro, Transport Properties of Fluids*, Cambridge, University Press, 1996

[2] **J.H. Ferziger, H.G. Kaper**: *Mathematical Theory of Transport Processes in Gasses*, North-Holland Publishing Company, London, 1972

[3] **F.R.W.McCourt, J.J. Beenakker, W.E. Köhler, I. Kuscer**: *Nonequilibrium Phenomena in Polyatomic gases*, Clarendon Press, London, 1990

[4] **S. Chapman, T.G. Cowling**: *The Mathematical Theory of Non-Uniform Gases*, Third Edition, Cambridge, University Press, 1970

[5] **P.D. Neufeld, A.R. Janzen, R.A. Aziz**: *Empirical Equations to Calculate 16 of the Transport Collision Integrals for the Lennard-Jones (12-6) Potential*, The Journal of Chemical Physics, Vol.57, No.2, pp. 1100-1102

[6] **T.-H. Chung, L.L. Lee, K.E. Starling**: *Applications of Kinetic Gas Theories and Multiparameter Correlation for Prediction of Dillute Gas Viscosity and Thermal Conductivity*, Ind. Eng. Chem. Res., Vol. 27, No. 4, pp. 671-659, 1988

[7] **N. Shibasaki-Kitajawa, M. Takahashi, C. Yokoyama**: *Viscosity of Gaseous HFC-134a Under High Pressures*, International Journal of Thermophysics, Vol.19, No. 5, pp.:1285-1295, 1998

[8] **M. Takahashi, N. Shibasaki-Kitajawa, C. Yokoyama**: *Viscosity of Gaseous HFC-125 Under High Pressures*, International Journal of Thermophysics, Vol.20, No. 2, pp.:445-453, 1999

[9] **C. Yokoyama, T. Nishino, M. Takahsashi**: *Viscosity of Gaseous Mixtures of HFC-125+HFC-134a under Pressure*, Fluid Phase Equilibria, Vol. 174, pp. 231-240, 2000

Journal of
Energy
Technology

ROTOR MECHANICAL STRESS ANALYSIS OF A DOUBLE-SIDED AXIAL FLUX PERMANENT MAGNET MACHINE

MEHANSKA ANALIZA ROTORJEV DVOSTRANSKEGA SINHRONSKEGA STROJA Z AKSIALNIM MAGNETNIM PRETOKOM

Franjo Pranjić[ℜ], Peter Virtič[1]

Keywords: Axial flux permanent magnet machine (AFPMM), mechanical stress analysis (MSA), rotor thickness

Abstract

This paper presents the mechanical stress analysis (MSA) of a rotor disk in a double-sided axial flux permanent magnet machine (AFPMM). The analysis considers the rotor of a prototype AFPMM with a double external rotor and single internal stator. Rotor disks of the prototype AFPMM are constructed of two 11.6 mm-thick steel disks and represent around 50% of the total weight of the machine. The new rotor disk thickness was determined based on a rotor axial displacement due to the attractive force between the permanent magnets on opposite rotor disks.

Povzetek

Članek predstavlja mehansko analizo rotorjev dvostranskega sinhronskega stroja s trajnimi magneti in aksialnim magnetnim pretokom. Analiziran je rotor prototipa stroja, ki ima dvojni zunanji rotor ter notranji stator. Rotor analiziranega stroja je izdelan iz dveh 11,6 mm debelih

---

ℜ Corresponding author: Franjo Pranjić, Tel.: +386 3 777402, Mailing address: Koroška cesta 62a, E-mail address: franjo.pranjic@um.si

[1] University of Maribor, Faculty of Energy Technology, Hočevarjev trg 1, 8270 Krško

jeklenih diskov, kar predstavlja približno 50% skupne teže stroja. Trajni magneti na nasproti ležečih rotorskih diskih povzročajo pritezne sile med rotorskimi diski, ki se posledično upognejo. Na podlagi upogiba rotorskih diskov pa je določena nova debelina le-teh.

1   INTRODUCTION

Axial flux permanent magnet machines have been becoming increasingly popular lately due to their compactness, high degree of reliability, efficiency, simple construction and high-power density, *[2-6]*. This type of machine is also called "a disk-type machine" and has various topologies:

- Single-sided (one stator and one rotor)
- Double-sided (single stator-double rotor or single rotor-double stator)
- Multistage (multiple rotors and stators).
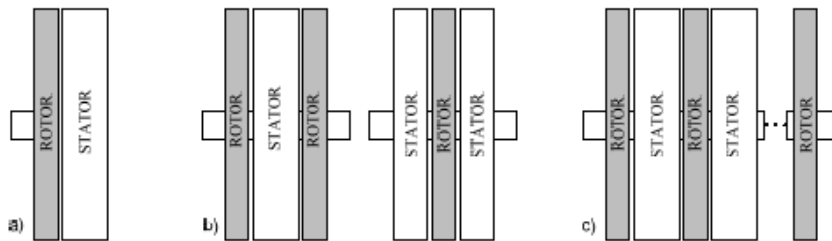
Figure 1: Basic topologies of AFPMM: a) single-sided, b) double-sided, c) multistage

All the above-mentioned topologies can be constructed with or without iron cores (coreless) and with surface-mounted or buried permanent magnets (PMs). Low power permanent magnet machines are usually constructed with coreless stators and steel rotors with surface mounted PMs, *[1]*.

Each machine topology has its own strengths and weaknesses. Topologies without stator cores are used for low- and medium-power generators and have various advantages, including the absence of cogging torque, as well as their linear torque-current characteristics, high power density, and compact construction. Due to the absence of the core losses, these types of generators can operate with a higher efficiency compared to the conventional generators, *[7]*.

Mechanical stress analysis (MSA) has been presented in several publications. In *[9]*, the authors present the MSA for a high-speed AFPMM and analyse the stress level of the rotor disks due to the high-speed rotation, using the three-dimensional finite element method (3D FEM). Fei et al. present the simplified 2D and 3D FEM for analysis and design of rotor disks of high-speed AFPM generators in *[10]*. Rani et al. present the computational method of rotor stress analysis for conventional rotors using J-MAG software in *[11]*. In *[14]*, the authors presented the structural analysis of low-speed axial-flux permanent-magnet machines.

Virtič, *[12]*, analysed the rotor disk thickness of the same prototype AFPMM concerning the magnetic flux density magnitudes.

This article firstly presents the double-sided AFPMM with an internal coreless stator and two external rotors and its characteristics, with a focus on the selected dimensions of rotor disks. The

prototype AFPMM was analytically analysed in *[7]* and optimized in *[8]* by using evolutionary optimization with a genetic algorithm and an analytical evaluation of objective functions. Since the thickness of the rotor disks was not included in the optimization (due to the assumed infinite permeability), this article presents the mechanical stress analysis (MSA) of the rotor disks used in the prototype machine and, based on the results, a new rotor disk thickness is determined.

The mechanical stress analysis in this article is accomplished by:

1. analytically calculating the pressure caused by the PMs on opposite disks and the attractive force between them,
2. simulating the stress distribution and deflection of the disks with Solidworks software based on the calculated magnetic pressure and force,

The primary reason for the rotor optimization lies in the fact that the weight of the two rotor disks represents about 50% of the total weight of the machine, *[1]*.

2   AFPMM PROTOTYPE

The AFPMM considered in this article is a double-sided AFPMM with two external rotors and one internal coreless stator. Figure 2 shows the geometric parameters, and Table 1 shows the optimized data of the analysed prototype AFPMM.
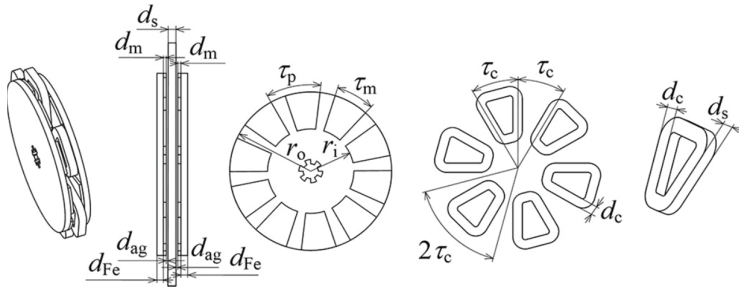
***Figure 2**, [8]: Geometric parameters of the AFPMM*

The PMs used in the prototype AFPMM are neodymium magnets (NdFeB). Figure 3 shows the PMs; their characteristics are presented in Table 2, where:

- B_r is the remanent magnetic flux density,
- H_{cB} is the coercive magnetic field intensity of the magnetic flux density,
- H_{cJ} is the coercive magnetic field intensity of the polarization,
- $(BH)max$ is the maximum energy product, and
- T_{max} is the maximum working temperature of PMs
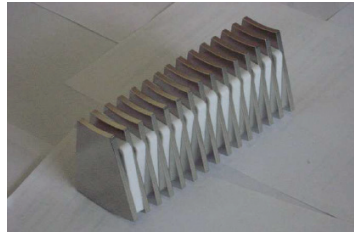
Figure 3, *[17]:NdFeB permanent magnets used in the prototype AFPMM*

Table 1: *GEOMETRY AND PARAMETERS OF ANALYSED AFPMM*

	Symbol	Quantity	Value/Unit
ROTOR	R	Rotor disk radius	150 mm
	d_{Fe}	Rotor disk thickness	11,6 mm
	d_M	Permanent magnet thickness	5 mm
	τ_m	Magnetic pole pitch	25°
	R_{iPM}	Inner radius of PM	80 mm
	R_{oPM}	Outer radius of PM	150 mm
	B_r	Remanent magnetic flux density	1,22 T
	τ_p	Pole pitch	36 °
	p	Number of pole pairs	5
STATOR	I	Rated phase current	12,3 A
	A	Electrical current density	5 A/mm^2
	P	Rated power at 1500 min^{-1}	4,4 kW
	N	Number of turns per coil	50
		Number of coils	12 (2x6)
	d_c	Coil width	20 mm
	d_s	Stator thickness	15 mm
	τ_c	Coil pitch	30°
	m	Number of phases	3
	d_{ag}	Air-gap thickness	1mm
	S_w	Copper wire cross section	2,46 mm^2

Table 2: *PROPERTIES OF PERMANENT MAGNETS USED IN PROTOTYPE AFPMM*

Type of PM	B_r		H_{cB}	H_{cJ}	$(BH)_{max}$		T_{max}
	(T)		(kA/m)	(kA/m)	(kJ/m³)		(°C)
	min	max			min	max	
38SH	1,22	1,25	907	1592	287	310	150

2.1   Stator design

The internal stator is constructed from non-magnetic polypropylene square plate with dimensions of 400×400×15mm. Each side of the plate has a carved space for six coils, four thermocouples, and slots for the conductors (Figure 4a). After the conductors are inserted in the slots, a varnish is applied, and the stator is ready for mounting (Figure 4b).

a)   b)
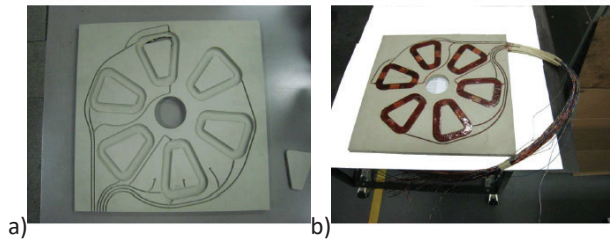
Figure 4, [17]*: a) Stator support structure, b) Stator ready for mounting*

2.1   Rotor design

Rotor disks are constructed from structural steel (St52), which has adequate magnetic properties and a suitable price. From the safety point of view, the thickness selected for the disks was 12 mm. After balancing, the final thickness was 11.6 mm.

a)   b)
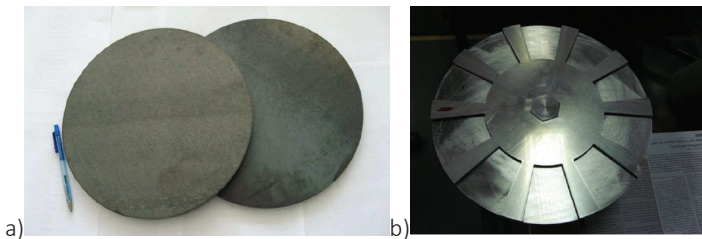
Figure 5, [17]*: a) Unbalanced rotor disks, b) Balanced rotor disk with an accessory for gluing the PMs on the rotor disk*
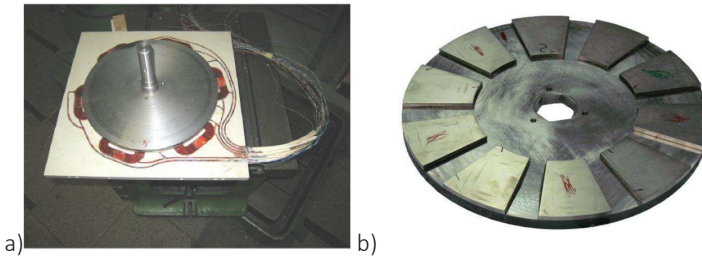
Figure 6, [7]**:** *a) Stator and double rotor with the shaft, b) Rotor disk with PMs*

3   METHODS AND RESULTS

The mechanical stress analysis was performed numerically and analytically, using the Solidworks simulation tool.

Solidworks software simulates the magnetic pressure of the PMs on the rotor disk and determines the stress distribution and deflection using the Finite Element method (FFEPlus, i.e. Fourier Finite Element Plus algorithm).

In finite element analysis, a problem is represented by a set of algebraic equations that must be solved simultaneously. FFEPlus is an iterative method that solves the equations using approximate techniques; a solution is assumed for each iteration, and the associated errors are evaluated. The iterations continue until the errors become acceptable, *[13]*.

Since the attractive forces of PMs are high, the deflection of the disk must not be too high due to the safety reasons, such as preventing the PMs from crashing into stator surface, preventing distortion of the air gap and consequently the characteristics of the prototype AFPMM.

3.1   Parameter selection and calculation

Maxwell stress is the link between electromagnetic and structural designs. It is represented by the magnetic attraction force acting between the rotor disks. Classical analysis of magnetic equivalent circuits can be used to determine the airgap flux density and hence the Maxwell stress is given by *[14]*:

$$q = \frac{B_{\mathrm{d}}^2}{2\mu_0} \tag{3.1}$$

where B_{d} is the airgap flux density and μ_0 - permeability of free space ($4\pi*10^{-7}$ Vs/Am) [14]. The magnetic flux density in the air gap is determined by equation (3.2) [1]:

$$B_{\mathrm{d}} = \frac{B_{\mathrm{r}}}{1 + \left(d_{\mathrm{ag}} + 0,5 d_{\mathrm{S}} \right) \dfrac{\mu_{\mathrm{rec}} k_{\mathrm{sat}}}{d_{\mathrm{M}}}} \tag{3.2}$$

$$k_{\mathrm{sat}} = 1 + \frac{l_{\mathrm{Fe}}}{2\mu_{\mathrm{r}} \left(d_{\mathrm{ag}} + 0,5 d_{\mathrm{Fe}} \right)} \tag{3.3}$$

$$\mu_{rec} = \frac{1}{\mu_0}\frac{\Delta B}{\Delta H} \tag{3.4}$$

where B_d is the magnetic flux density in the air gap, B_r is the remenent magnetic flux density of the PM, d_{ag} is the air gap thickness, d_s is the stator thickness, d_{Fe} is the rotor disk thickness, d_M is the PM thickness, k_{sat} is the saturation factor for iron, μ_r is the permeability of the steel, μ_{rec} is the relative recoil permeability, which is determined with the data of the magnets in Table 2.

The attractive force between PMs on opposite disks can be calculated as magnetic pressure multiplied by the active surface area of all PMs S_{PM} as shown in *[1]*:

$$F = \frac{B_d^2}{2\mu_0}\left(S_{PM}\right) \tag{3.5}$$

$$S_{PM} = \alpha_i \frac{\pi}{4}\left(D_{out}^2 - D_{in}^2\right) \tag{3.6}$$

$$\alpha_i = \frac{\alpha_{PM}\, 2p}{360} \tag{3.7}$$

Where α_i is the coefficient that is calculated with the angle of PMs multiplied by the number of PMs per rotor disk (poles) and divided by 360 degrees.

Using the previously-described equations, data needed for the simulation was determined as shown in Table 3.

Table 3: *GEOMETRY AND PARAMETERS OF ANALYSED AFPMM*

Symbol	Quantity	Value/Unit
q	Magnetic pressure caused by the PMs	74496 Pa
S_{PM}	Active area of all PMs	0,0351 m^2
F	Attractive force between rotor disks	2615 N
d_m	Permanent magnet thickness	5 mm
B_d	Peak value of magnetic flux density in the air gap	0,4327 T
d_{ag}	Air-gap thickness	1mm
d_s	Stator thickness	15 mm
μ_{rec}	Relative recoil permeability	1,0704
k_{sat}	Saturation factor	1,02

3.2   Simulation

First, the simulation of the stress analysis and deflection was performed for the 11.6 mm rotor disk thickness. The simulation itself included the entire rotor for the accuracy of the results since in many articles the analysis includes only a segment of the rotor.

The force between PMs on opposite rotor disks was applied on each magnet on the simulated rotor disk. Figures 7a and 7b show the Von Mises stress distribution on the rotor disk and the displacement for 11.6 mm rotor thickness, respectively. It is clear that the rotor thickness can be reduced from the mechanical point of view since the maximum deflection is only 0.0053 mm.

After a few simulations, it was determined that the 7 mm rotor thickness would be sufficient to withhold the forces between the adjacent PMs on opposite disks in such a way that the deflection remains acceptable.

Figures 8a and 8b show the Von Mises stress distribution on the rotor disk and the displacement of 7 mm rotor disk thickness, respectively. It can be seen from Figure 8a that the simulated deflection is 0.2171mm.

In *[12]*, the author analysed the rotor disk thickness for this prototype AFPMM concerning the magnetic characteristics of the machine and determined that the characteristics are acceptable at 7 mm rotor thickness since there is practically no difference between magnetic flux density magnitudes calculated at 7 mm and 11.6 mm of rotor disk thickness. The simulation in Solidworks shows the same result for the mechanical point of view.

a)   b)
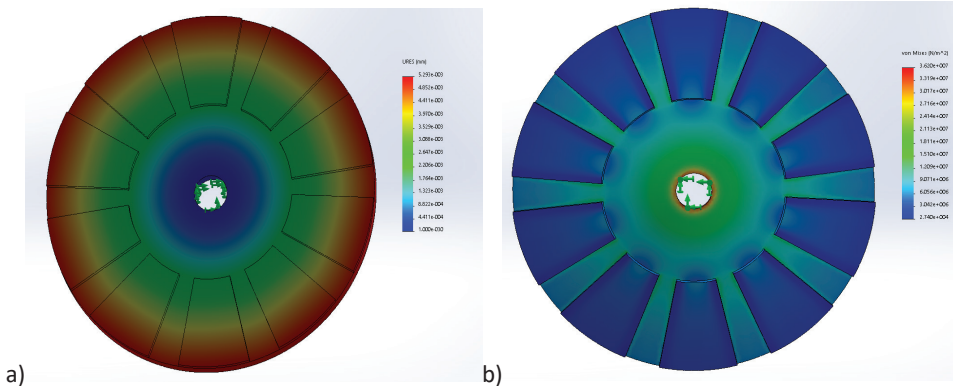
Figure 7: *11,6 mm rotor thickness: a) deflection, b) Von Mises stress distribution*

a)   b)
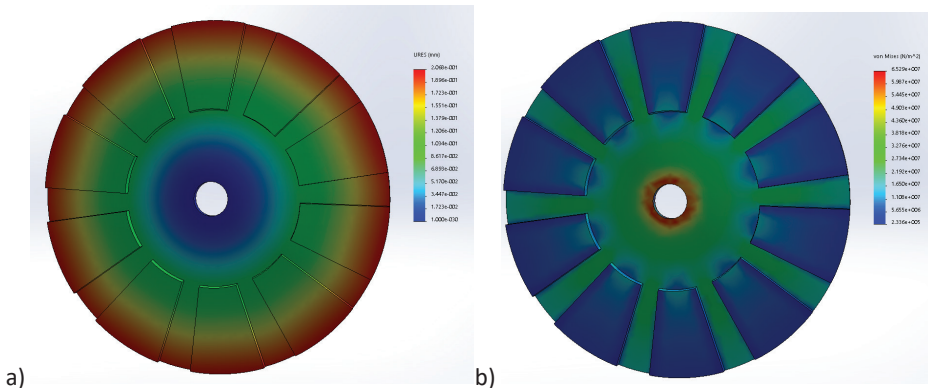
Figure 8: *7 mm rotor thickness: a) deflection, b) Von Mises stress distribution*

3.3   Analytical verification

Equations for bending circular plates are derived in *[15]* and *[16]*. Timoshenko, *[15]*, derived the differential equations for symmetrical bending of circular plates from observing the symmetrically distributed load acting on a circular plate.

In *[16]*, the authors presented equations for various types of loads on a circular plate. Figure 10 shows the case that is suitable for a rotor disk of AFPMM with surface mounted PMs.
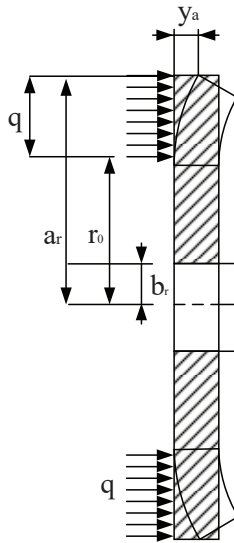
Figure 9: *Circular plate bending*

Equations for deflection calculations are:

$$y_a = M_{rb} \frac{a_r^2}{D} C_2 + Q_b \frac{a_r^3}{D} C_3 + q \frac{a_r^4}{D} L_{11}$$

(3.8)

$$M_{rb} = \frac{-q a_r^2}{C_8} \left(\frac{C_9}{2 a_r b_r} \left(a_r^2 - r_0^2 \right) - L_{17} \right)$$

(3.9)

$$Q_b = \frac{q}{2 b_r} \left(a_r^2 - r_0^2 \right)$$

(3.10)

$$C_2 = \frac{1}{4} \left(1 - \left(\frac{b_r}{a_r} \right)^2 \left(1 + 2 \ln \left(\frac{a_r}{b_r} \right) \right) \right)$$

(3.11)

$$C_3 = \frac{b_r}{4 a_r} \left(\left(\left(\frac{b_r}{a_r} \right)^2 + 1 \right) \ln \left(\frac{a_r}{b_r} \right) + \left(\frac{b_r}{a_r} \right)^2 - 1 \right)$$

(3.12)

$$C_8 = \frac{1}{2} \left(1 + v + (1 - v) \left(\frac{b_r}{a_r} \right)^2 \right)$$

(3.13)

$$C_9 = \frac{b_r}{a_r} \left(\frac{1 + v}{2} \ln \left(\frac{a_r}{b_r} \right) + \frac{1 - v}{4} \left(1 - \left(\frac{b_r}{a_r} \right)^2 \right) \right)$$

(3.14)

$$L_{11} = \frac{1}{64} \left(1 + 4 \left(\frac{r_0}{a_r} \right)^2 - 5 \left(\frac{r_0}{a_r} \right)^4 - 4 \left(\frac{r_0}{a_r} \right)^2 \left(2 + \left(\frac{r_0}{a_r} \right)^2 \right) \ln \left(\frac{a_r}{r_0} \right) \right)$$

(3.15)

$$L_{17} = \frac{1}{4} \left(1 - \frac{1 - v}{4} \left(1 - \left(\frac{r_0}{a_r} \right)^4 \right) - \left(\frac{r_0}{a_r} \right)^2 \left(1 + (1 + v) \ln \left(\frac{a_r}{r_0} \right) \right) \right)$$

(3.16)

$$D = \frac{E t^3}{12 \left(1 - v^2 \right)}$$

(3.17)

Table 4 presents the variables used in the set of equations (3.8)-(3.17) and their values.

Values of abovementioned variables are presented in Table 4 for a 7 mm rotor disk thickness.

Table 4: *Variables used for deflection calculation*

Symbol	Quantity	Value/Unit	
y_a	Deflection of rotor disks	0.20129 mm	
M_{rb}	Bending moment	469 Nm	
a_r	Outer radius of the disk	150 mm	
b_r	Inner radius of the disk	15 mm	
r_0	Radial location of unit line loading or start of a distributed load	80 mm	
D	Constant termed the "flexural stiffness" or "flexural rigidity",	6513 Pa mm^3	
Q_b	Unit shear force (force per unit of circumferential length)	39979 Pa mm^2/mm	
q	Magnetic pressure	74496 Pa	
$C_2, C_3\ C_9$	Plate constants dependent upon the ratio a=b	C_2	0.2425
		C_3	0.0005
		C_9	0.0818
L_{11}, L_{17}	Loading constants dependent upon the ratio a=r0	L_{11}	0.015994568091594
		L_{17}	0.112680595325043
v	Poisson's ratio	0,28	
E	Elastic module of the material used for rotor disks	210 GPa	
t	Thickness of the circular plate (rotor disk).	7 mm	

Using the equations described above, 0.20129 mm deflection was calculated for the 7 mm thick rotor disk. Magnetic pressure q was reduced by a factor that takes into account the area of magnets (multiplied by a coefficient αi) since it is not constant over the area as marked on Figure 9.

Compared to the results obtained via the simulation, we can see that there is only 2.66% difference which is acceptable.

3   CONCLUSION

Using the Solidworks software and a set of analytical equations a new rotor disks thickness was determined for the analysed prototype AFPMM. MSA showed that, from a mechanical point of view, the existing rotor disks thickness can be reduced to 7 mm and maintain sufficient stiffness, so the air gap does not change significantly. By changing the thickness of the rotor disks, the weight of disks is reduced by approximately 40%.

References

[1]   **Gieras JF, Wang RJ, Kamper MJ:** *Axial Flux Permanent Magnet Brushless Machines,* Springer Verlag, 2008

[2]   **W. Fei, P. C. K. Luk, and K. Jinupun:** *Design and analysis of high-speed coreless axial flux permanent magnet generator with circular magnets and coils*, Electr. Power Appl. IET, vol. 4, no. 9, pp. 739–747, 2010

[3]   **Xue, Y., Han, L., Li, H., Xie, L.**: *Optimal design and comparison of different PM synchronous generator systems for wind turbines*, Int. Conf. Electrical Machines and Systems, pp. 2448–2453, 2008

[4]   **Pinilla, M., Martinez, S.**: *Selection of main design variables for low-speed permanent magnet machines devoted to renewable energy conversion*, IEEE Trans. Energy Convers., 26, (3), pp. 940–945, 2011

[5]   **M. Mirsalim, R. Yazdanpanah, and P. Hekmati:** *Design and analysis of double-sided slotless axial-flux permanent magnet machines with conventional and new stator core*, IET Electr. Power Appl., vol. 9, no. 3, pp. 193–202, 2015

[6]   **H. Hatami, M. Bagher, B. Sharifian, and M. Sabahi**: *A New Design Method for Low-Speed Torus Type Afpm Machine for Hev Applications*, IJRET, Volume: 02 Issue: 12, pp. 396–406, 2013

[7]   **P. Virtič, P. Pišek, T. Marčič, M. Hadžiselimović and B. Štumberger:** *Analytical Analysis of Magnetic Field and Back Electromotive Force Calculation of an Axial-Flux Permanent Magnet Synchronous Generator with Coreless Stator*, IEEE Transactions on Magnetics, vol. 44, no. 11, pp. 4333–4336, 2008

[8]   **P. Virtič, M. Vražić, and G. Papa:** *Design of an axial flux permanent Magnet synchronous machine using analytical method and evolutionary optimization, IEEE Trans. Energy Convers.*, vol. 31, no. 1, pp. 150–158, 2016

[9]   **S. Kumar, T. A. Lipo, and B. Kwon**: *A 32,000 rev/min axial flux permanent magnet machine for energy storage with mechanical stress analysis*, IEEE Trans. Magn., vol. 52, no. 7, pp. 1–1, 2016

[10]   **W. Fei, P. C. K. Luk, and T. S. El-Hasan**: *Rotor integrity design for a high-speed modular air-cored axial-flux permanent-magnet generator*, IEEE Trans. Ind. Electron., vol. 58, no. 9, pp. 3848–3858, 2011

[11]   **J. A. Rani, E. Sulaiman, M. F. Omar, M. Z. Ahmad, and F. Khan**: *Computational Method of Rotor Stress Analysis for Various Flux Switching Machine Using J-MAG*, IEEE Student Conference on Research and Development (SCOReD), 721–726, 2015

[12]   **P. Virtič**: *Analysis of rotor disk thickness in coreless stator axial flux permanent magnet synchronous machine*, PRZEGLĄD ELEKTROTECHNICZNY, vol. ISSN 0033, no. 12, pp. 12–15, 2012

[13]   2015 Solidworks Help Documentation

[14]   **M.A. Mueller, A.S. McDonald and D.E. Macpherson:** *Structural analysis of low-speed axial-flux permanent-magnet machines*, IEE Proceedings-Electric Power Appl., vol. 152, no. 6, pp. 1417–1426, 2005

[15]   **S. Timoshenko:** *Theory of Plates and Shells*, Second edition, 1987, McGraw-Hill Book Company, ISBN 0-07-064779-8

[16]   **W. C. Young and R. G. Budynas:** *Roark's Formulas for Stress and Strain*, vol. 7, no. 7th Edition. 2002

[17]   **P. Virtič:** *Načrtovanje in analiza sinhronskih strojev s trajnimi magneti in aksialnim magnetnim pretokom*, Doctoral thesis, University of Maribor, 2009

Nomenclature

(Symbols)	(Symbol meaning)
R	rotor disk radius
d_{Fe}	rotor disk thickness
d_M	permanent magnet thickness
τ_m	magnetic pitch
R_{iPM}	inner radius of PM
R_{oPM}	outer radius of PM
B_r	remanent magnetic flux density
τ_p	pole pitch
p	number of pole pairs
I	rated phase current
A	electrical current density
P	rated power at 1500 min-1
N	number of turns per coil
d_c	coil width

d_s	stator thickness
τ_c	coil pitch
m	number of phases
d_{ag}	air-gap thickness
S_W	Copper wire cross section
B_d	airgap flux density
μ_0	permeability of free space
d_d	fictitious air gap thickness
k_{sat}	saturation factor for iron
μ_r	permeability of the steel
μ_{rec}	relative recoil permeability
S_{PM}	active surface area of all PMs
α_i	coefficient that is calculated with angle of PMs multiplied by the number of PMs per rotor disk (poles) and divided by 360 degrees
q	magnetic pressure
F	attractive force between adjacent magnets
y_a	deflection of rotor disks
M_{rb}	bending moment
a_r	outer radius of the disk
b_r	inner radius of the disk
r_0	radial location of unit line loading or start of a distributed load
D	stiffness factor of the material
Q_b	unit shear force (force per unit of circumferential length)
$C_2, C_3\ C_9$	plate constants dependent upon the ratio a=b
$L_{11},\ L_{17}$	loading constants dependent upon the ratio a=r0
v	Poisson's ratio
E	elastic module of the material used,
t	thickness of the circular plate (rotor disk)

FUTURE GENERATION IV SMR REACTORS: ASSESSMENT AND POSSIBILITY OF INTEGRATION IN CLOSED NUCLEAR FUEL CYCLES

PRIHAJAJOČA IV. GENERACIJA SMR REAKTORJEV: EVALVACIJA IN MOŽNOST INTEGRACIJE V ZAPRTE JEDRSKE GORIVNE KROGE

Aleš Buršič ℜ Tomaž Žagar[1]

Keywords: small and medium size reactors, generation IV reactors, investment cost, value analysis methodology, review and evaluation process, modular design, advanced nuclear fuel cycle, energy transition, sustainability

Abstract

Over the previous decade, many economic, strategic, technical, and other arguments in favour of Small and medium-size reactors (SMR), present in the nuclear industry since the beginning of its use for peaceful purposes, have become prominent. The Generation IV SMR is a next-generation design excelling in its considerable contribution to sustainability. Most favourable concepts impose high coolant temperatures and high breeding ratios and represent progress in the design of future GEN IV SMRs. This paper presents a new review and evaluation process of SMR GEN IV reactors, which seem most suitable for early implementation. Evaluation presented in this paper was performed on the basis of the Value Analysis methodology, indicating the most economically interesting technologies with the shortest time to commercial availability. The SMR GEN IV reactor integration in advanced closed nuclear fuel cycles could an play important role in the energy transition to sustainable oriented

ℜ Corresponding author: Aleš Buršič, GEN energija, d.o.o., Vrbina 17, 8270 Krško, Slovenia, Tel.:+ 386 7 49 10 250, E-mail address: ales.bursic@gen-energija.si

[1] GEN energija, d.o.o., Vrbina 17, 8270 Krško, Slovenia

low-carbon energy future. Mass balance and material flow for nuclear fuel cycles involving SMRs were established with the NEA 1767 SMAFS model and through the webKORIGEN software. The advantages of SMRs attract embarking countries to look towards use of nuclear as domestic energy source, especially when the paradigm of energy independence is becoming strategically important.

<u>Povzetek</u>

V preteklem desetletju se pojavljajo številni ekonomski, strateški, tehnični ter ostali razlogi, ki kažejo na določene prednosti Majhnih in srednjih reaktorjev (SMR), sicer prisotnih od pričetka uporabe jedrske energije za miroljubne namene. Četrta generacija jedrskih elektrarn med katere spadajo tudi SMR GEN IV je vključena v napredne zaprte gorivne kroge in omogoča velik napredek v trajnostnem razvoju ter proizvodnji energije. Najobetavnejši SMR koncepti stremijo k visoki temperaturi hladila na izstopu iz sredice ter visokem oplodnem razmerju ter predstavljajo velik napredek v zasnovi SMR GEN IV reaktorjev prihodnosti. Ta članek predstavlja sodoben pristop k procesu pregleda in evalvacije SMR GEN IV reaktorjev, ki so glede na današnje vedenje in informacije najugodnejši za zgodnjo implementacijo. V tem članku predstavljena evalvacija bazira na metodologiji vrednostne analize ekonomsko najzanimivejših tehnologij z najkrajšim časom do njihove komercialne uporabe. Vključevanje SMR GEN IV reaktorjev v sodobne zaprte gorivne cikle predstavlja velik potencial pri energetski tranziciji v nizkoogljično prihodnost. Masne bilance in tok materiala v izbranih gorivnih ciklih, primernih za implementacijo SMR reaktorjev, so bile določene s pomočjo NEA 1767 SMAFS modela ter v nadaljevanju s pomočjo webKORIGEN programskega paketa. Predstavljene prednosti SMR reaktorjev so zanimive tudi za države, ki razmišljajo prvič o uporabi jedrske energije, saj postaja energetska samozadostnost ter neodvisnost strateško zelo pomembna.

1   INTRODUCTION

Small and Medium Reactors (SMR) have been present in nuclear industry since the beginning of its use for electricity or heat generation in the 1950s (Figure 1).
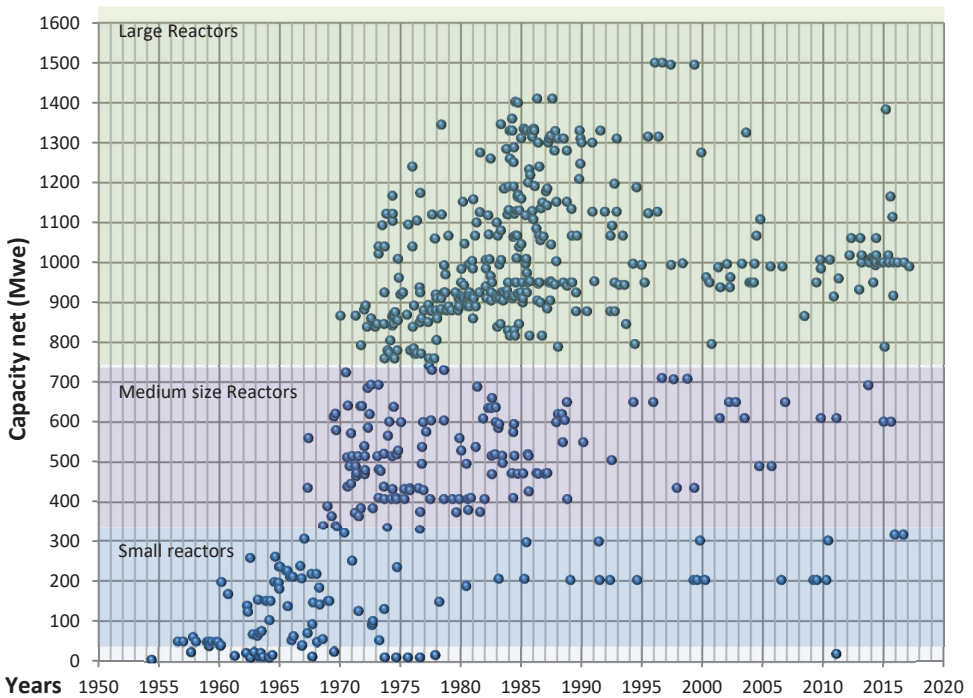

Figure 1: *Size of operating Nuclear Power Plants including SMRs, data source, [28]*

1.1   SMR implementation goals

SMR units are designed as single units that can also be accommodated as multiple SMR modules sequentially on single sites to optimize site investment costs. Economics of smaller units is planned as increasing the factory assembly manufacturing of units, shorter construction times, optimized supply chains and as mass production impact at manufacturing equipment modules could reduce construction costs and further overnight costs.

SMR investment costs include the engineering, procurement and construction (EPC) costs and the owner's costs. The total capital investment cost (TCIC, defined in *[2]*) is equal to the sum of overnight costs, contingency and the cost of financing, *[1]*. According to available data for SMR overnight costs, the prices of electricity predicted per installed kW (USD/kWe) are in range from 1200 to 4000 USD/kWe, *[4]*. This is a rough estimate and involves many volatile factors.

1.1.1 SMR general design features

SMRs are intended to fill market niches with implementation in smaller grids, or where heat production or desalinization in addition to electricity is foreseen. SMR is expected to have simpler design, optimized manufacturing costs and due to its size optimized TCIC in comparison with large ALWRs. SMRs are mainly designed with high levels of passive safety. For instance, a SMR reactor vessel with smaller thermal power (P_{therm}) and higher thermal inertia can be by its design narrow and high, thus enabling more intensive natural recirculation with higher thermal dissipation with higher coolant flows along the fuel channels. With higher secondary coolant parameters, more advanced thermodynamic cycles with higher turbine efficiency rates can be implemented. It can be concluded from an American Nuclear Society report, that a major part of the active safety systems and support systems implemented in large ALWRs ($P_{electr} > 600\ MWe$) is redundant for SMRs and can be effectively replaced by passive approaches, *[5]*.

1. 1. 2 General GEN IV reactors classification

Among next-generation design reactors, Generation IV (GEN IV) reactors generally excel in sustainability, minimal environmental impacts, better economy, and further reduced proliferation issues.

Figure 2 presents six GEN IV technologies, according to their breeding ratios and coolant temperatures at reactor core exit. The most favourable concepts impose high coolant temperatures and high breeding ratio, thus most effectively implementing three fields of progress in the design of future reactors:

- higher coolant temperatures when exiting reactor core enabled with the use of new materials and advanced thermodynamic cycle's higher turbine efficiency rates,

- high neutron flux with 100 times better UO fuel efficiency, less radioactive waste and use of reprocessed fuel from LWRs,

- favourable breeding ratio; fissile material obtained to spent fissile material after the use of a fuel mixture of fissile and fertile material in a reactor or ratio between fission and capture in actinides.
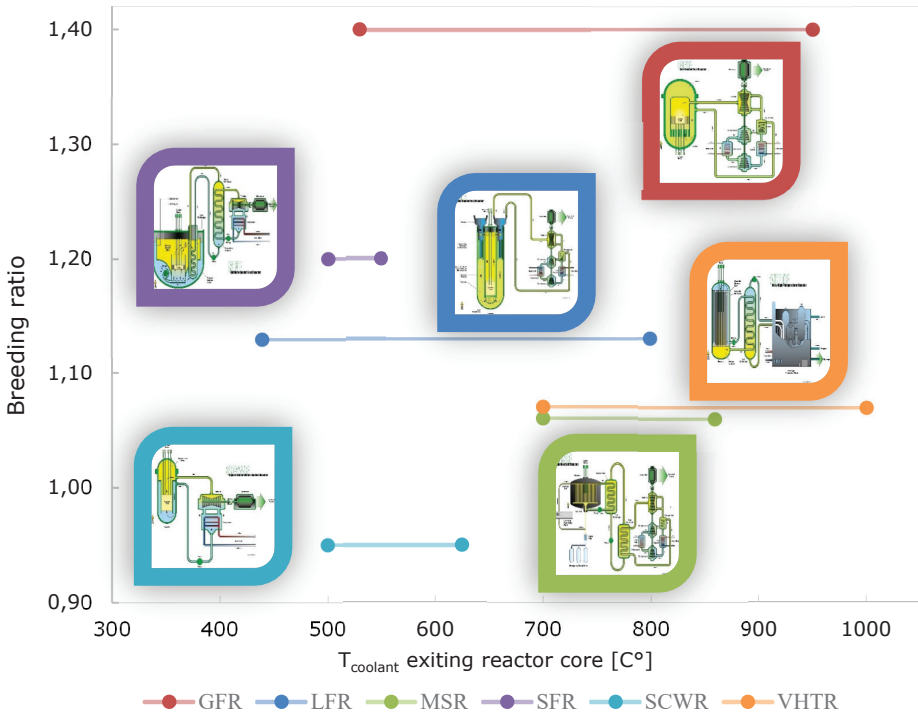
Figure 2: *six most promising GEN IV SMR technologies as suggested by Generation IV International Forum, data sources: [6], [7], [8], [9], [10], [11], [12], [13], [14], [15], [16]*

2   GENERAL APPROACH TO SMR MODULARITY

A common approach to most SMR reactor designs, especially GEN IV designs is based on the elimination of postulated initiating events (PIE) and the prevention of severe accident consequences, mainly by passive means. A combination of passive and active safety systems is often used for other accident prevention approaches, similar as in today's GEN III ALWRs, such as AP1000, VVER-1000, ESBWR, etc.

According to many SMR designers, general features contributing to the efficient implementation of inherent and passive safety design are:

- larger surface to volume ratio at reactor vessel for larger decay heat removal, especially in case of a single-phase coolant,

- solutions for a more compact Reactor Coolant System (RCS) as for instance integral compact RCS pool, suppressing certain initiating events,

- reduced power density of reactor core, simplifying implementation of passive safety systems,

- reduced potential hazard results from lower source term due to lower fuel inventory, lower heat and pressure energy stored in the reactor, and lower integral decay heat rate, [19].

2. 1 Modularization process and improvement possibilities

Customer requirements, the existence and further development of modularization at construction or manufacturing are triggered and preserved by the requirements of a short construction schedule, cost reduction, higher quality and safety at the construction site and in exploitation phase (nuclear safety). Those factors emerging mostly from market demands like investor requirements at NPP construction or vendors requirements to achieve more competitive position on market. They are integrated within the whole product lifecycle; in this case, the lifecycle of Systems Structures and Components (SSC) and for the whole NPP project from construction to decommissioning (Figure 3).

In the case of SMRs, modularity is present on two levels: an SMR unit, as a whole, represents a module designed to fit and operate within multi-unit site; modules within an SMR are compatible and interchangeable within unit or within units from different vendors.
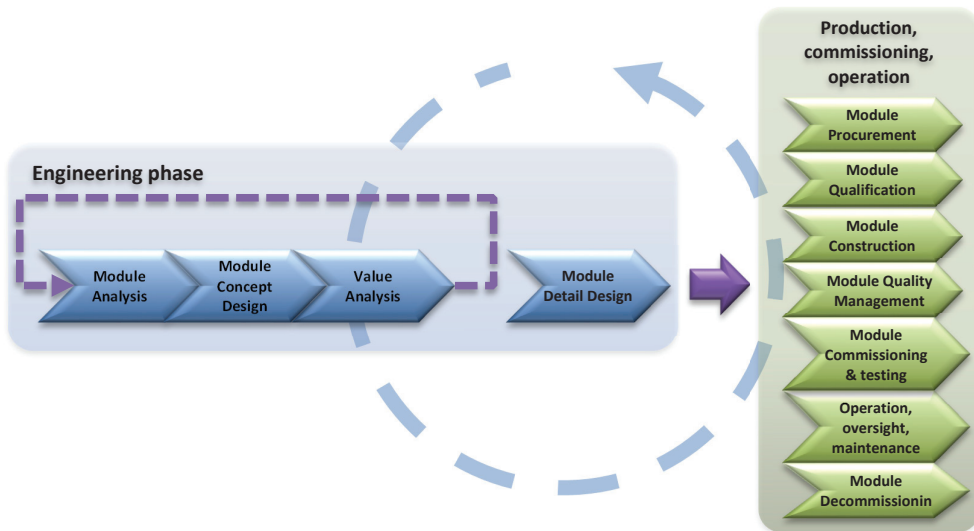

Figure 3: *Modularization process integrated within module lifecycle*

2. 1. 1 SMR SSC Modularity from the designer's point of view

Since SMRs are in various design phases, it is difficult to predict to what extent particular SSCs will be interchangeable within various vendor types of SMR, as has been the case for many decades in other industries like automotive, aerospace, naval, robotics, etc. At such a modularity stage, where common SSCs were developed and licensed, a designer would have easier task to make system integration of those SSC. In the nuclear industry, in addition to functionality requirements, there is additional requirement for nuclear safety, which is distinct from other industries and of great importance in setting design basis for the plant.

The following list covers some potential SSCs that might be common for sodium-cooled fast Reactors of various vendors. SSCs of various manufacturers could be compatible, having the same functionality and operating parameters; all could be used in the same SFR or one SSC that is functionality compatible with the required operating parameters of SFRs from different vendors:

- Steam Generator (SG), with which modularity/similarity is achieved with adequate heat transfer surface, SG design remains unchanged and covers wider group of this SMR type with different power outputs, e.g. with one or more same SGs;

- Electromagnetic Reactor Coolant Pumps (RCP), controlled with frequency converters, enabling pre-set, project-defined optimum coolant flow through various operating states, as a single RCP or multiple-mounted, similar to AP1000 design;

- RCS piping, forged according to unified codes and standards with appropriate multiple sizes, covering the range of reactors, according to safety requirements, forged as a monobloc; standardisation lowers the manufacturing costs;

- Auxiliary reactor vessel cooling systems could be unified and pre-licensed for the whole range of FSR SMRs; various power ranges are handled with multiple, yet redundant systems;

- Fuel Handling Building (FHB) could be assembled from the same or similar modules, varying according to requirements with modular support equipment;

- Seismic resilience, small and compact dimensions at SMRs with higher eigen-frequencies are more favourable for consideration on siting in more demanding geological, geotechnical and seismic locations, with additional implementation of appropriate seismic isolators, it should be viable that site properties would not exist as limiting factor even when considering those reactors on the most demanding sites.

Other equipment, such as intermediate heat exchangers, reactor protection system modules, sodium reservoirs, steam and other pipelines, and equipment for transformation to electric energy, can be similarly optimized, modularized, and unified.

Experiences with the modularization process show that not many efforts in this direction have been successful, especially when the process itself has been the responsibility of developers or suppliers, without clear and strong support and collaboration from investors/operators with high requirements and particularly regulatory bodies, which may have to expand their scope and participate more proactively in order to promote the safe and peaceful use of atomic energy.

3   REVIEW AND EVALUATION OF PROMISING SMR GEN IV REACTORS

A review and evaluation process of SMR GEN IV reactors that seem most suitable for early implementation is divided into two phases: preliminary elimination and secondary elimination selection. Evaluation methodology is qualitative with elements of value analysis (VA), *[20]*, according to the methodology of Small Modular Reactor Strategic Assessment, *[21]*, and is divided into five steps within those phases:

1. collecting relevant information on assessed technologies,

2. preliminary elimination,

3. determination of important functions and properties,

4. properties and relative variant value assessment,

5. optimal technology selection.

The intermediate result based on VA is a ranked list of SMRs. The selection of a technology group is made among those reactors according to the most collected points for suggested ranking factors and characteristics for the most promising technology, (1st part of 4th phase). The goal of the review process by assessing the economy of different technologies is to define, by VA (2nd part of 4th phase), the group of technologies that meets the set threshold of ranking factors and characteristics (5th phase).

3. 1 Technology relevant data acquisition

Data from 27 SMR GEN IV technologies (reactor designs from specific vendor) being in various design phases were gathered for the assessment:

- 7 types of Gas-cooled fast reactors (GFR),

- 1 very-high-temperature reactor (VHTR),

- 9 types of lead-cooled fast reactors, cooled with Pb or Pb-Bi eutectic (LFR),

- 3 types of molten-salt reactors (MSR),

- 7 types of sodium-cooled fast reactor (SFR).

The listed technologies are in development in the US, Russian Federation, Japan, China, India, South Korea, Czech Republic, and South Africa. Most R&D institutions or companies do not publish or reveal their progress regularly; therefore, this assessment is based on publicly available articles, industry societies, conferences, NRC or IAEA evaluations, interviews with design engineers or other available sources, referenced at the end of the paper.

3. 2 Preliminary elimination

Preliminary elimination evaluates each of the 27 technologies according to following parameters:

- commercial operation is viable only after 2030,

- complex process of fuel fabrication; remark: this parameter is important, but has less influence in this preliminary evaluation due to different design phases of assessed technologies,

- unreliable or non-existent sources for R&D financing, high risk for financing termination,

- FOAK technology, proof-of-concept working prototype is required before final prototype,

- technology in early R&D phase.

Any technology fulfilling any of the above parameters is excluded (✖) as an unsuitable candidate for further assessment. An exception is made when, within the whole technology group (GFR, VHTR, etc.) there is no suitable technology, in which case one technology is conditionally (☑)

selected, having the best result within the group. According to these rules, the following technologies were selected and presented in Table 1.

Table 1: SMR GEN IV reactor overview [1], [2], [4], [19], [21]

Technology designation	Selection	Power (MWe)	Designer	Origin	Parameters, Remarks
GFR (Gas-cooled Fast Reactor) group					
Adams Engine	✘	1 to 100	Adams Atomic Engines, Inc.	USA	a, b, e
EM2	✘	240	General Atomic	USA	a, b
GT-MHR	✘	150	General Atomic, OKBM Afrikantov, Fuji	USA, Russian Federation, Japan	a, b, e, *igt*
ALLEGRO	☑	75 (MWt)	ÚJV Řež, a.s., MTA EK in VUJE a.s., CEA, EURATOM	Europe	a, b, c, d, e
MTSPNR	✘	2	NIKIET	Russian Federation	a, b, c, double reactor unit
PBMR	✘	150	PBMR, Pty.	South Africa	a, c
GTHTR-300	✘	280	JAERI	Japan	a, b
VHTR/AHTR (Very High Temperature Reactor) group					
Antares	✘	~288	Areva, Fuji	France, Japan	e, b, d
HTR-PM	✔	211	INET, Tsinghua University	China	
LFR (Lead-cooled Fast Reactor) group					
ANGSTREM (Pb-Bi)	✘	n/p	TES-M		*noinf*
BREST-OD-300	✘	300	Gidropress	Russian Federation	e
ENHS	✘	50	University of California, Berkley	USA	a
HPM(Pb-Bi)	✘	25	Hyperion Power Generation, Inc.	USA	e single or multiple reactor unit
LSPR(LBE)	✘	53	RLNR TITech	Japan	a
SSTAR (Pb-Bi)	✘	20 10 to 100	Argonne National Lab & Lawrence Livermore Laboratory, Toshiba	USA,	e
STAR-LM, STAR-H2 Hydrogen production	✘	180	Argonne National Lab & Lawrence Livermore Laboratory	USA, Japan	e
SVBR-100 (Pb-Bi)	✔	100	Gidropress	Russian Federation	*dd*
TWR	✘	300	Lawrence Livermore Lab (DOE), Terrapower	USA	a, b, d, e
ALFRED	✘	300	Ansaldo nuclear with 16 European organizations	Europe	a, b, e
MSR (Molten Salt Reactor) group					
Fuji MSR (LFTR)	☑	100	IThEMS	Japan, Czech Republic	a, d, e

Technology designation	Selection	Power (MWe)	Designer	Origin	Parameters, Remarks
LFTR	✖	20 to 50	Flibe Energy	USA	a, b, *noinf*
PB-AHTR	✖	410	UC Berkley, ORNL	USA	a, b, d, e
SFR (Sodium-cooled Fast Reactor) group					
4S	✔	10	Toshiba	Japan	*dd*
ARC-100	✖	100	Advanced Reactor Concepts, LLC	USA	e
CEFR	✔	20	CNEIC	China	*op*
KALIMER-600	✖	600	KAERI	South Korea	a, b
PFBR-500	✔	500	IGCAR	India	*const*
PRISM	✔	155	GE, Hitachi	USA, Japan	*dd*
Rapid-L	✖	0.2	Toshiba, CRIEPI, JAERI	Japan	a, b, *igt*
Astrid	✖	600	CEA with industry consortium	International	a, b, e

Remarks: *igt*-integral gas turbine poses great technological challenges, *noinf*-non-existent or poor information on technology, *dd*- reactor in detail design phase, *const*-reactor in construction phase, *op*-reactor in operation phase.

Technologies are conditionally selected for secondary elimination based on larger development potential, are recognized as interesting for potential investors in FOAK technologies or have broad international support on financing and R&D and have large potential for niche markets.

3. 3 Secondary elimination

Eight SMR designs entered the secondary phase: Allegro, HTR-PM, SVBR-100, Fuji SMR, 4S, CEFR, PFBR-V and PRISM. The second elimination step consists of the following phases of VA: 3) determination of important functions and properties, 4) properties and relative variant value assessment (USD/kW $_{installed}$), and 5) optimal technology selection.

3. 3. 1 Determination of important functions and properties

In this phase, the functions, properties and properties influence of SMR technologies enabling evaluation are selected. Results of 8 SMR technologies evaluated in greater detail on the design, licensing and construction with characteristics are:

1. Design maturity and status of development, *[22], [23],*

2. Designer, manufacturer experiences, *[22], [23],*

3. Licensing challenges, regarding current GEN III challenges at licensing, *[22], [23],*

4. Simplicity of design and constructability, *[22],*

5. Technical and technology challenges,

6. Level of participation in closed fuel cycle, HLW amount in fuel elements, possibility for the use of reprocessed nuclear fuel from other technologies like PWR, BWR, *[22], [24],*

7. Maturity levels for supply chain, and infrastructure for components and heavy component manufacturing and supply.

At VA, product properties, in this case technologies (variants), are evaluated. Because most of the assessed technologies are in various phases (e.g. R&D, construction, etc.), it is necessary not to assess only properties, which may be changed during process, but also the effects and influence due to conditions at project development over certain aspects, such as design or economics, etc. Instead of specific properties, the combination of group of properties as a whole (influenced properties field) are important and therefore evaluated.

3. 3. 2 Properties and relative variant value assessment

3. 3. 2. 1 Variant properties assessment

Technologies are evaluated by assessing the fulfilment level of factor K of selected group of properties for technology and influenced properties field, varying from factor value from:

- 0.00 – inadequate, influence on assessment field gives unacceptable results,

- e.g. 0.50 – appropriate, without significant influence on assessment field,

- 1.00 – most suitable, influence on assessment field exhibits excellent results.

Since all assessment fields may not be equally important to the assessor, they can be weighted with a ponder value. The sum of denominated ponder relative values for assessment fields evaluated with K represents 100%; therefore, change in one ponder changes the influence of all other ponders for specific variants.

Variant properties assessment was conducted on the basis of pre-prepared assessment sheets by a group of five nuclear technology experts, three of them with doctorates in nuclear technology and two with more than five decades of experience in SSC design since the deployment of GEN II NPPs. Table 2 summarizes their evaluations of selected variants. The number of points of selected property group at variant is arithmetic mean of assessor's evaluations:

$$\bar{T} = \frac{1}{n}\sum_{i=1}^{n} T_i \ , \ for \ n = N^o \ of \ assessors \tag{3.1}$$

Table 2: Variant properties and influenced properties field assessment results [22]

N°	Property / Influenced Properties Field	Ref.	Allegro $\Sigma p_i/n$ [%]	$\Sigma K_i/n$	$\Sigma T_i/n$	HTR-PM $\Sigma p_i/n$ [%]	$\Sigma K_i/n$	$\Sigma T_i/n$	SVBR-100 $\Sigma p_i/n$ [%]	$\Sigma K_i/n$	$\Sigma T_i/n$	Fuji MSR $\Sigma p_i/n$ [%]	$\Sigma K_i/n$	$\Sigma T_i/n$
1	Design maturity and status of development	[22]	18.2	0.6	9.9	18.2	0.8	14.9	18.2	0.9	15.3	18.2	0.3	5.9
2	Designer, manufacturer experiences	[22]	13.4	0.6	7.8	13.4	0.7	8.4	13.4	0.8	11.1	13.4	0.3	3.7
3	Licensing challenges	[22]	14.2	0.5	7.0	14.2	0.7	9.2	14.2	0.8	11.5	14.2	0.3	4.4
4	Simplicity of design and constructability	[22]	14.4	0.5	7.9	14.4	0.5	6.6	14.4	0.7	9.3	14.4	0.5	7.5
5	Technical and technology challenges	[22]	12.1	0.7	7.8	12.1	0.8	10.5	12.1	0.9	10.8	12.1	0.5	5.7
6	Level of participation in closed fuel cycle	[24]	14.4	0.7	9.4	14.4	0.3	4.8	14.4	0.7	9.7	14.4	0.3	4.0
7	Maturity of supply chain and manuf. infrastr.		13.3	0.7	9.3	13.3	0.9	11.6	13.3	0.9	11.7	13.3	0.5	5.9
	Eval. Sum all fields ΣT				59.18			66.00			79.30			37.21
	Rank				VII			VI			I			VIII

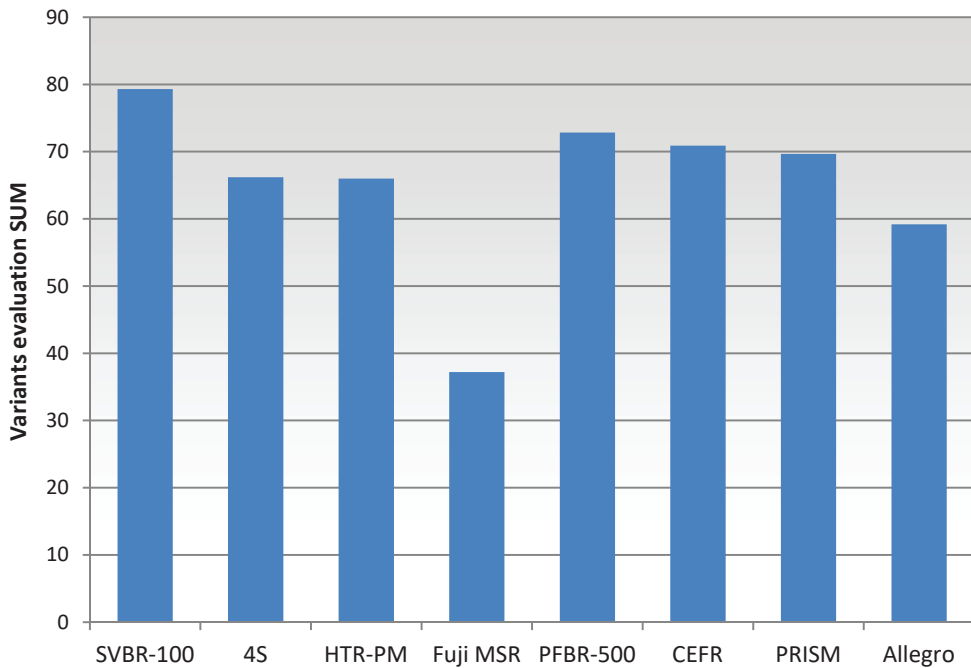| N°	Property / Influenced Properties Field	Ref.	4S $\Sigma p_i/n$ [%]	$\Sigma K_i/n$	$\Sigma T_i/n$	CEFR $\Sigma p_i/n$ [%]	$\Sigma K_i/n$	$\Sigma T_i/n$	PFBR-500 $\Sigma p_i/n$ [%]	$\Sigma K_i/n$	$\Sigma T_i/n$	PRISM $\Sigma p_i/n$ [%]	$\Sigma K_i/n$	$\Sigma T_i/n$
1	Design maturity and status of development	[22]	18.2	0.7	12.8	18.2	0.8	14.4	18.2	0.8	14.8	18.2	0.8	13.8
2	Designer, manufacturer experiences	[22]	13.4	0.8	10.4	13.4	0.7	8.9	13.4	0.8	9.9	13.4	0.8	10.1
3	Licensing challenges	[22]	14.2	0.6	8.4	14.2	0.7	9.7	14.2	0.8	11.0	14.2	0.6	8.6
4	Simplicity of design and constructability	[22]	14.4	0.6	8.0	14.4	0.5	7.5	14.4	0.5	7.1	14.4	0.6	7.8
5	Technical and technology challenges	[22]	12.1	0.7	9.0	12.1	0.8	10.8	12.1	0.8	10.9	12.1	0.8	10.8
6	Level of participation in closed fuel cycle	[24]	14.4	0.6	8.5	14.4	0.6	8.5	14.4	0.6	8.8	14.4	0.6	8.9
7	Maturity of supply chain and manuf. infrastr.		13.3	0.7	9.1	13.3	0.8	11.0	13.3	0.8	10.5	13.3	0.7	9.7
	Eval. Sum all fields ΣT				66.20			70.90			72.85			69.67
	Rank				V			III			II			IV

Figure 4: Variant assessment results' ranking, *[22]*

3. 3. 2. 2 Relative value at assessed variants

Collecting information on technology implementation (investment) costs is an essential part of the comprehensive assessment, although it is focused on a niche industrial field prone to ever-changing competition conditions. Collected information originates from publicly available information, *[4]*, or from discussion with leading experts in nuclear, SMR technology-related fields. Regardless of the source of information, it can be concluded with certainty that the information is more reliable than cost calculations executed for particular SMR SSC, especially when experience shows that even partial costs given to recognized reliable investors by vendors in bidding phases for NPPs may vary from the final costs. Equipment costs may also vary according to investors requirements, since investors can prefer specific equipment suppliers due to fleet/equipment standardization and maintenance optimization, even if not recognized as standard OEM by vendors. Power generation plant costs also depend and vary on specific investor requirements, such as desalinization, hydrogen production, heat cogeneration, etc., and are not included due to multiple variants emerging from those requirements. Further costs that should be recognized in assessment are contingency, project engineering, licensing costs, various compensations costs to local community, municipality or state etc.

Cost are presented separately in Table 3, ranking is conducted according to Levelized Unit Electricity Cost (LUEC) and to overnight capital costs of each technology, *[4]*.

When assessing variant suitability, relative values are calculated, *[20]*:

$$V = {}^{F}\!/_{C} = {}^{P}\!/_{C} = {}^{T}\!/_{C} = {}^{properties}\!/_{costs} \tag{3.2}$$

Where V represents relative value, F function, P property (group), costs (LUEC and overnight capital costs separately) and T variant properties value. Calculated V (Figure 5) provides information on property group assessment with variants relative value under costs consideration, where higher value represents better results, having lower costs.

Table 3*: Relative value according to LUEC and to overnight capital costs*

	HTR-PM	SVBR-100	Fuji MSR	4S
Overnight Capital Costs (OCC)	1500 USD	1200 USD	4500 USD	1500 USD
Relative tech. value/OCC	0.0440	0.0661	0.0083	0.0441
Levelized Unit Electricity Cost (LUEC)	51 USD/MWh	42 USD/MWh	29 USD/MWh	290 USD/MWh
Relative tech. value/LUEC	1.2940	1.8882	1.3056	0.2283
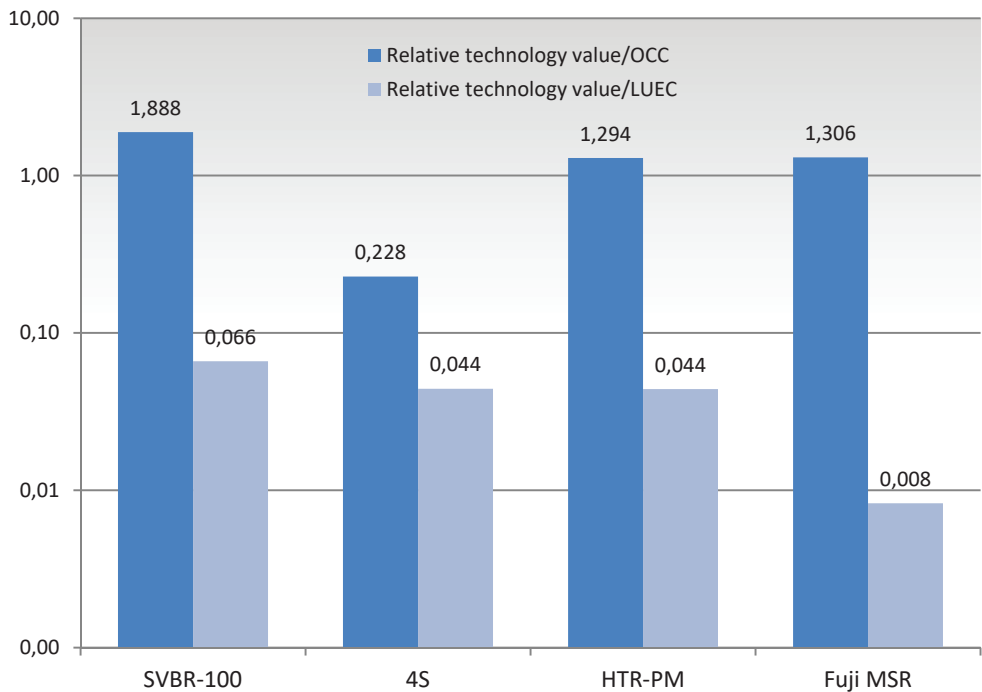
Figure 5*: Relative value ranking from Table 3*

Assessment approach with Value Analysis is reasonable and useful in case of strategic investor decisions, especially when dealing with larger lifecycles of investment, such as with NPPs. Assessment results indicate the most economically interesting technologies with the shortest times to commercial availability.

4   SMR GEN IV INTEGRATION IN ADVANCED NUCLEAR FUEL CYCLES

Suitable for SMR GEN IV integration are examples of advanced, fully closed, nuclear fuel cycles (NFC, FC), in which all actinides are continuously recycled in fast reactors. Only two fuel cycle schemes were studied in this paper (out of several different fuel cycles possible) and are indicated as FCA and FCB.

A fuel cycle based on PWR reactor and integral fast reactor concept (Fuel Cycle A (FCA)), featuring partitioning & transmutation (P&T) option, results in small waste quantities without actinides, containing only material from reprocessing losses and fission products (FP). In FCA, proliferation possibility is disabled, since there is no Pu separation from other actinides (Figure 6).

A fuel cycle based on GCR concept (Fuel Cycle B (FCB)), capable of burning all actinides (U, Pu, Am, Cm, etc.) results in minimising actinides loss in process and maximizing use of uranium resources. Waste is trans-uranium elements from reprocessing efficiency losses and FP. Due to the small consumption of depleted uranium, FCB can be recognized as a sustainable energy source (Figure 8).

The FCA fuel cycle features a PRISM reactor, and FCB features an ALLEGRO reactor. Material flow and mass balances originate from the characterization of advanced nuclear fuel cycles and the determination of HLW quantity for final disposal, *[24]*, with the consideration of the Slovenian case on used nuclear fuel inventory, *[27]*. Mass balance and material flow for the beginning of fuel cycle was determined for each NFC through the NEA 1767 SMAFS model. With an iteration approach through webKORIGEN software, final mass balances of Used Nuclear Fuel (UNF) were established. The activity, toxicity, residual heat power, and mass balance of final high-level waste (HLW) for final disposal were also established with the same approach through webKORIGEN. Quantities in both NFCs were normalized on 1MWe year/FC, *[24]*.
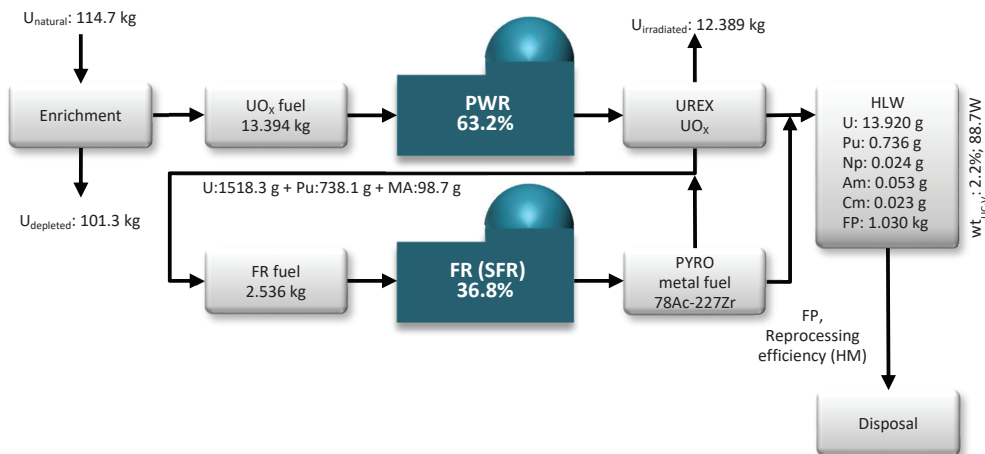

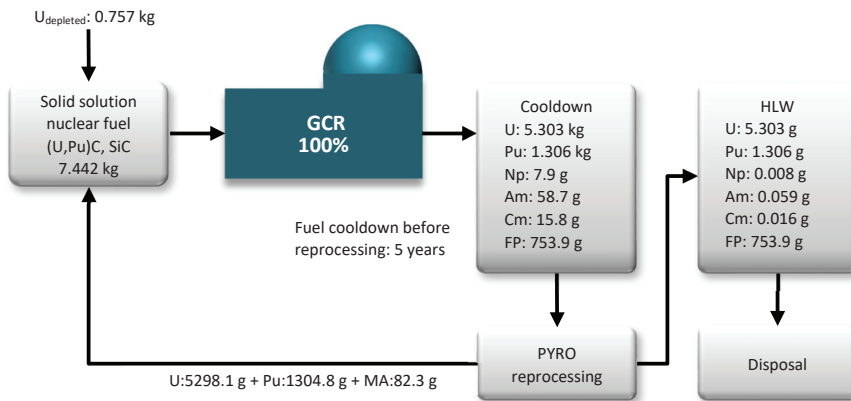*Figure 6: FCA fuel cycle, UOX (UREX) reprocessing, Pyrochemical reprocessing of metal fuel (PYRO)-TRU partitioning and homogenic transmutation, [24]*

SMR GEN IV reactors could play an essential role in the energy transition to sustainable oriented low-carbon energy future. Combining reprocessing within closed or semi-closed FCs minimizes

the quantity (volume) of material entering NFC and waste. In addition, there is notable improvement with minimizing relative residual heat generation and radioactivity reduction in comparison with open FC (Figure 7 for FCA, Figure 9 for FCB and Figure 10 for FCA, FCB, FCO comparison). All features combined contribute to reducing necessary volume in final disposal and its decay time to natural background level. Since economy of smaller HLW disposals is worse than of larger, the idea of establishing regional HLW disposal, accommodating fuel from many international reactors could be more attractive, especially when disposing of reprocessed HLW, for which the radiotoxicity timespan down to natural background could degrade under 1000 years.
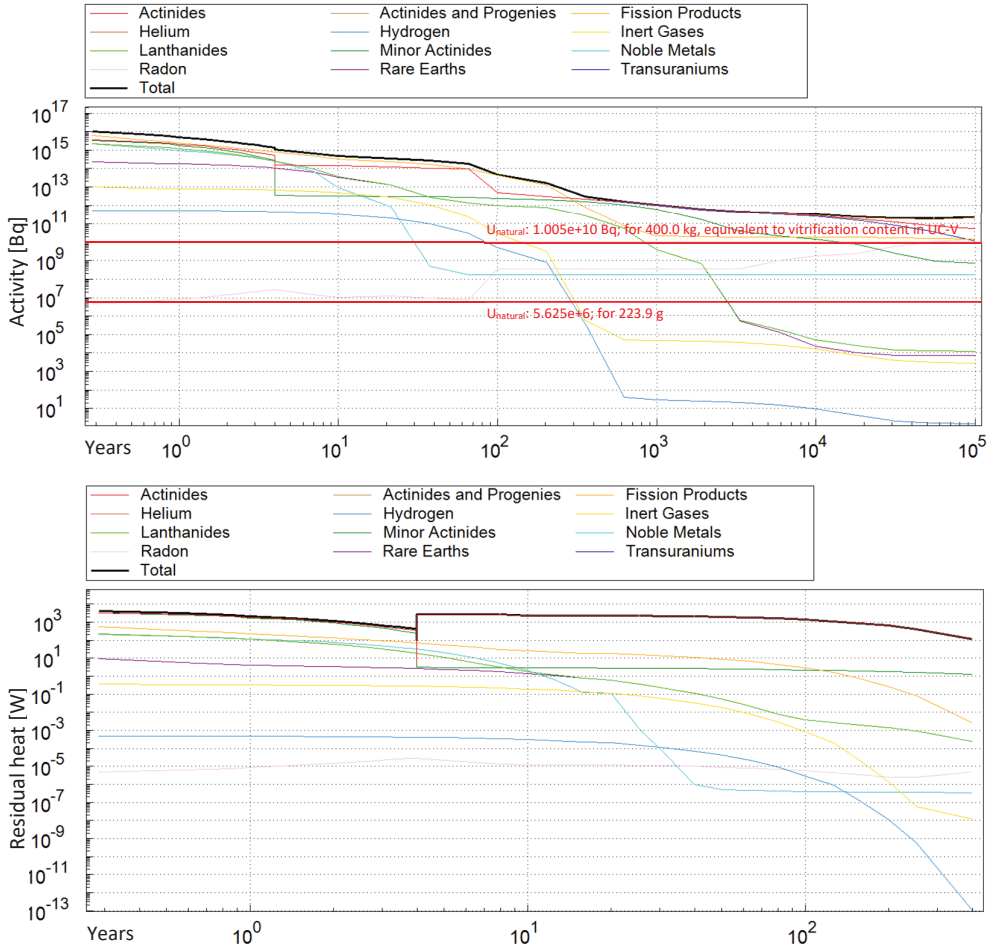
Figure 7: *Activity and residual heat decay over time for FCA fuel cycle after disposal, [24]*

Figure 8: *FCB fuel cycle, Pyrochemical reprocessing of metal fuel (PYRO)-TRU partitioning and homogenic transmutation, [24]*
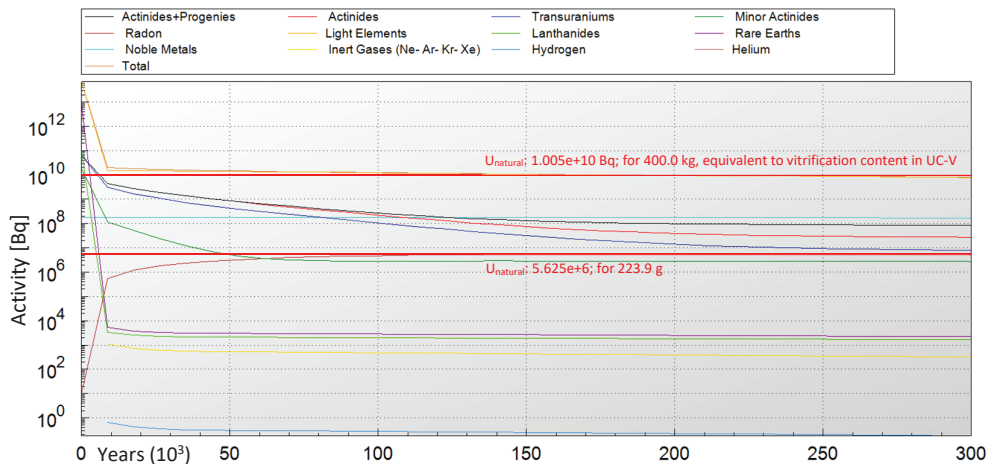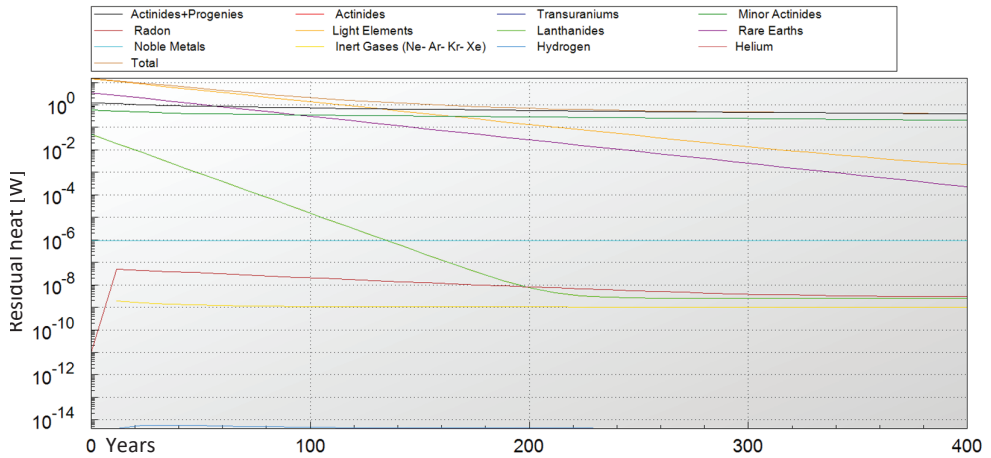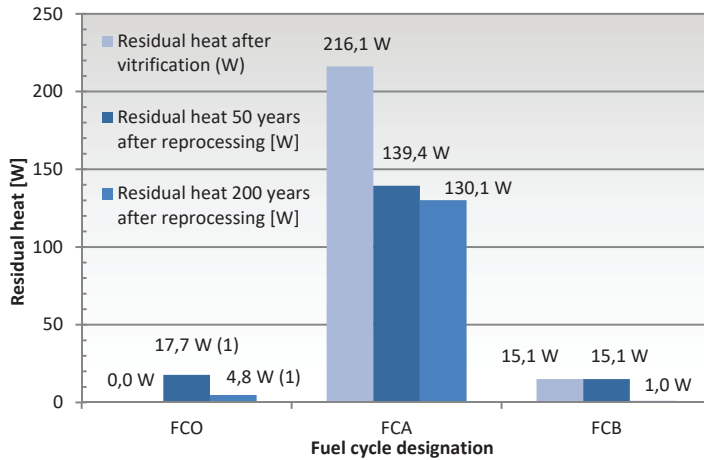
Figure 9*: Activity and residual heat decay over time for FCB fuel cycle after disposal [24]*

Figure 10 compares SMR-suitable FCA and FCB with open fuel cycle featuring the once-through use of UNF in PWRs designated FCO (Fuel Cycle – Open). Residual heat at FCO is generated in the disposed fuel element without any reprocessing. According to the disposed mass of material, the relative residual heat at reprocessed HLW is more favourable; however, at vitrification in universal canisters (UC-V), attention should be paid to the maximum allowable heat load for the glass matrix. In addition to residual heat generation, the heat load for the glass matrix is dependent on the environment contact conditions and exposure.
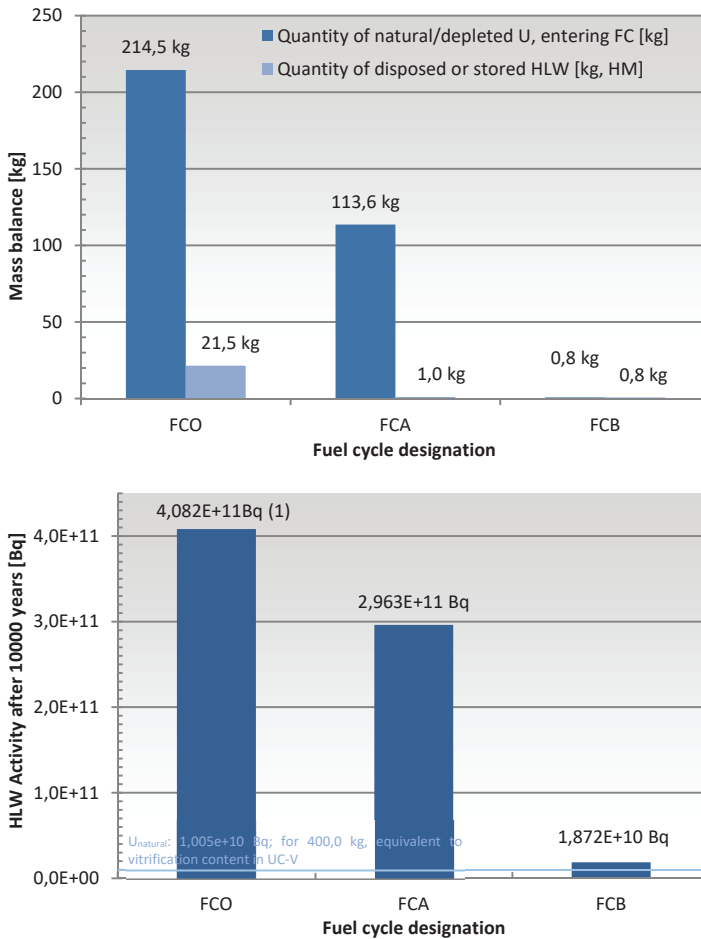
Figure 10: Mass balance, Residual heat decay and Activity over time, comparing open fuel cycle FCO to closed CFA and FCB, [24]

5   CONCLUSION

The main technological advantages of SMRs over large ALWRs emerge primarily out of the size of nuclear steam supply system (NSSS) and other SSCs. Size of SMRs and their potential for modularity enables factory assembly manufacturing of SMR units. This brings shorter construction times, more effective and efficient quality assurance/quality control and optimization of the project structure and management that can reduce investment capital costs. In many cases, SMR SSCs involve FOAK technology solutions, which may be extremely innovative, such as minimizing the quantity of necessary SSCs while simultaneously maintaining safety levels in comparison with large GEN II or GEN III+ reactors. In contrast, with the FOAK approach, designers implement unproven technology and increase the risk of delayed commercial availability.

The main contribution and novelty of this paper is its value analysis review and the evaluation of 27 different SMR GEN IV reactors design currently available. This value analysis gives insight into the commercially most promising technologies with strong implementation potential, which could be economically interesting in the next 10 to 15 years.

Eight out of 27 evaluated SMR designs were shortlisted in the first phase of evaluation. Those technologies went through a more detailed assessment. The most points were collected by the SVBR-100 SMR design (lead-cooled fast reactor designed in Russia). On the second and third places are PFBR-500 and CEFR SMR designs (Sodium-cooled Fast Reactor from India and China, respectively). Among the so-called "western technologies", on the fourth place, PRISM SMR (sodium-cooled fast reactor designed by GE and Hitachi) shows potential, especially due to its multifunctionality and robust seismic design.

Based on available information, despite their unfavourable economy of scale, SMR overnight investment costs put SMRs cost of electricity production in the upper band of the price range of large reactors. Since the calculated cost of electricity production is based on predictions, actual economics is yet to be proven after first SMRs are put into operation.

When summarizing SMR technology could experience future growth under several conditions:

- similar or lower overnight investment costs and electricity production costs in comparison to large reactors,

- high level of external modularity with ability to efficiently connect several reactors on site offering several exploitation possibilities, internal modularity and standardization of SSCs of similar SMRs from different suppliers,

- flexibility at siting, with no or minimal environmental impact, seismic robustness, suitability for siting close to populated areas, smart grid and distributed supply integration possibility,

- unified international licensing approach implementation based on experience on SMR licensing conducted by world's most recognized regulatory bodies, such as US NRC, STUK, ASN,

- large flexibility and impact at integration into existing nuclear fuel cycle schemes, consequentially leading towards closed nuclear fuel cycle,

- ultimate inherent safety against internal and internal events, with minimal or no operator intervention and relying on advanced passive safety features.

In case SMRs fail to deliver promised and expected features, especially at economic issues, they will remain interesting solely for research and for investors with high budgets, intent to solve energy supply issues at remote locations with poor infrastructure but high value. Energy supply independence is becoming more and more important in the focus of many environmental agreements, energy transitions towards electrification in heating, transportation and other demands. SMR technologies could deliver some of the answers for future energy needs.

References

[1] **OECD/NEA, Nuclear Energy Agency, Small Modular Reactors**: *Nuclear Energy Market Potential for Near-term Deployment*, OECD Publications, NEA No. 7213, Paris, France, 2016

[2] **EMWG**: *Cost Estimating Guidelines for Generation IV Nuclear Energy Systems*, Generation IV International Forum (GIF), Economic Modelling Working Group, EMWG, 2007

[3] **D. Schlissel and B. Biewald:** *Nuclear Power Plant Construction Costs*, Synapse Energy Economics, Inc., Nuclear's Tangled Economics, Business Week, 2008

[4] **OECD/NEA**: *Current status, Technical Feasibility and Economics of Small Nuclear Reactors*, OECD Publications, Paris, France, 2011

[5] **ANS**: *Interim report of the American Nuclear Society President's special committee on Small and Medium Sized reactor (SMR)*, generic licensing issues, ANS, 2010

[6] **Gen4 Energy**: *The Gen4 Module (G4M)*, http://www.gen4energy.com/technology/, accessibility check Jan 2018

[7] **Peter Líška, VUJE, Gérard Cognet**: *CEA, The ALLEGRO project – European project of fast breeder reactor*, Proc. 1st International Nuclear Energy Congress, Warsaw, 23-24 may, 2011

[8] **A. Kumar et al**: *Analysis of a sustainable gas cooled fast breeder reactor concept,* Department of Nuclear Engineering, Texas A&M University, College Station, USA, 2014

[9] **E. Greenspan**: *Fission Reactors – Options and Challenges*, Department of Nuclear Engineering, University of California, Berkley, USA, 2007

[10] **Idaho National Laboratory**: *Generation IV Nuclear Energy Systems Ten-Year Program Plan - Fiscal Year 2007*, Appendix 6.0-MSR, USA, 2007

[11] **Z. Donghui**: *Fast Reactor Development Strategy in China*, China Institute of Atomic Energy, Proc. International Conference on Fast Reactors and Related Fuel Cycles, 4.-7. march, Paris, France, 2013

[12] **C. Barton**: *Advanced High Temperature Reactor*: http://nucleargreen.blogspot.com/2010/08/advanced-high-temperature-reactor.html, 2010, accessibility check Jan 2018.

[13] **GIF, GEN IV International forum**: *Generation IV Systems*: https://www.gen-4.org/gif/jcms/c_59461/generation-iv-systems, accessibility check Jan 2018.

[14] **Idaho National Laboratory**: *Generation IV Nuclear Energy Systems Ten-Year Program Plan - Fiscal Year 2007*, Appendix 2.0-SCWR, Idaho, USA, 2007

[15] **A.I. Filin**: *Design Features of BREST Reactors and experimental work to advance the concept of BREST Reactors*, SSC RF, RDIPE, Moscow, RF, 2003

[16] **A.V. Zrodnikov**: *Multipurposed Small Fast Reactor SVBR-75/100 Cooled by Plumbum-Bismuth*, SSC RF, IPPE, Obninsk, RF, 2003

[17] **D. J. Diamond**: *Generation IV Nuclear Energy Systems*, Brookhaven National Laboratory, presented at Tennessee University, USA, 2003

[18] **M. Ragheb**: *Nuclear, Plasma and radiation Science*, Part IV, Ch. 4 High Temperature Gas Cooled Reactor, University of Illinois, USA, 2014

[19] **IAEA**: *Designs Features to Achieve Defence in Depth in Small and Medium Sized Reactors*, IAEA Nuclear Energy Series Report NP-T-2.2, Wienna, 2009

[20] **M. Pšunder**: *The economy of construction industry*, Tehniška založba Slovenije, Ljubljana, 1991

[21] **Worley Parsons**: *Small Modular Reactor Strategic Assessment*, Reading, Avgust 2011

[22] **A.Buršič, T.Žagar**: *Generation IV SMR Reactor development Forced renaissance or true need?*, PhD research seminar at subject Nuclear Power Plant Technologies, PhD Programme Nuclear Energy and Technology, University of Maribor, Faculty for Civil Engineering, April 2015

[23] **IAEA**: *Status of Small and Medium Sized Reactor Designs*, IAEA, Division of Nuclear Power, Department of Nuclear Energy, Vienna, 2011

[24] **A.Buršič, T.Žagar**: *Characterization of Advanced Nuclear Fuel Cycles and determination of HLW quantity for final disposal based on Slovenian Used Nuclear Fuel Inventory*, PhD research seminar at subject Advanced fuel cycles, PhD Programme Nuclear Energy and Technology, University of Maribor, Faculty for Civil Engineering, May 2012

[25] **OECD/NEA**: *Advanced Nuclear Fuel Cycles and Radioactive Waste Management*, NEA No. 5990, OECD Publications, Paris, 2006

[26] **T. Žagar**: *Closed fuel cycle technologies*, Jožef Stefan Institute, IJS-DP-9762, Issue 1, Ljubljana, 2008

[27] **T. Žagar, A. Buršič et al**: *Recycling as an option of used nuclear fuel management strategy*, Nuclear engineering and design, ISSN 0029-5493, vol. 241, no. 4, Amsterdam, North-Holland, 2011

[28] **World Nuclear Association**: *Reactor Database*, http://www.world-nuclear.org /information-library/facts-and-figures/reactor-database.aspx, accessibility check Jan 2018

MAIN TITLE OF THE PAPER
SLOVENIAN TITLE

Author[1], Author [2], Corresponding author[ℜ]

Keywords: (Up to 10 keywords)

Abstract

Abstract should be up to 500 words long, with no pictures, photos, equations, tables, only text.

Povzetek

(Abstract in Slovenian language)

<u>Submission of Manuscripts:</u> All manuscripts must be submitted in English by e-mail to the editorial office at jet@um.si to ensure fast processing. Instructions for authors are also available online at http://www.fe.um.si/en/jet/author-instructions.html.

<u>Preparation of manuscripts</u>: Manuscripts must be typed in English in prescribed journal form (MS Word editor). A MS Word template is available at the Journal Home page.

A title page consists of the main title in the English and Slovenian language; the author(s) name(s) as well as the address, affiliation, E-mail address, telephone and fax numbers of author(s). Corresponding author must be indicated.

<u>Main title</u>: should be centred and written with capital letters (ARIAL bold 18 pt), in first paragraph in English language, in second paragraph in Slovenian language.

<u>Key words</u>: A list of 3 up to 6 key words is essential for indexing purposes. (CALIBRI 10pt)

<u>Abstract</u>: Abstract should be up to 500 words long, with no pictures, photos, equations, tables, - text only.

<u>Povzetek</u>: - Abstract in Slovenian language.

<u>Main text</u> should be structured logically in chapters, sections and sub-sections. Type of letters is Calibri, 10pt, full justified.

ℜ Corresponding author: Title, Name and Surname, Organisation, Department, Address, Tel.: +XXX x xxx xxx, E-mail address: x.x@xxx.xx

[1] Organisation, Department, Address

[2] Organisation, Department, Address

Chapter examples:

1   MAIN CHAPTER

(Arial bold, 12pt, after paragraph 6pt space)

1.1   Section
(Arial bold, 11pt, after paragraph 6pt space)

1.1.1 Sub-section

(Arial bold, 10pt, after paragraph 6pt space)

Example of Equation (lined 2 cm from left margin, equation number in normal brackets (section. equation number), lined right margin, paragraph space 6pt before in after line):

Equation   (1.1)

Tables should have a legend that includes the title of the table at the top of the table. Each table should be cited in the text.

Table legend example:

Table 1: *Name of the table (centred, on top of the table)*

Figures and images should be labelled sequentially numbered (Arabic numbers) and cited in the text – Fig.1 or Figure 1. The legend should be below the image, picture, photo or drawing.

Figure legend example:

Figure 1: *Name of the figure (centred, on bottom of figure, photo, or drawing)*

References

[1] **N. Surname:** *Title,* Journal Title, Vol., Iss., p.p., Year of Publication

[2] **N. Surname:** *Title,* Publisher, Year of Publication

[3] **N. Surname:** *Title* [online], Publisher or Journal Title, Vol., Iss., p.p., Year of Publication. Available: website (date accessed)

Examples:

[1] **J. Usenik**: *Mathematical model of the power supply system control*, Journal of Energy Technology, Vol. 2, Iss. 3, p.p. 29 – 46, 2009

[2] **J. J. DiStefano, A.R. Stubberud, I. J. Williams**: *Theory and Problems of Feedback and Control Systems*, McGraw-Hill Book Company, 1987

[3] **T. Žagar, L. Kegel:** *Preparation of National programme for SF and RW management taking into account the possible future evolution of ERDO* [online], Journal of Energy Technology, Vol. 9, Iss. 1, p.p. 39 – 50, 2016. Available: http://www.fe.um.si/images/jet /Volume 9_Issue1/03-JET_marec_2016-PREPARATION_OF_NATIONAL.pdf (7. 10. 2016)

Example of reference-1 citation: In text *[1],* text continue.

Nomenclature

(Symbols)	(Symbol meaning)
t	time